A Study of the Near Wake Deformation of the X-Rotor Vertical-Axis Wind Turbine With Pitched Blades

Bensason, David; Sciacchitano, Andrea; Giri Ajay, Adhyanth; Simao Ferreira, Carlos

DOI
10.1002/we.2944

Publication date
2024

Document Version
Final published version

Published in
Wind Energy

Citation (APA)
Bensason, D., Sciacchitano, A., Giri Ajay, A., & Simao Ferreira, C. (2024). A Study of the Near Wake Deformation of the X-Rotor Vertical-Axis Wind Turbine With Pitched Blades. *Wind Energy*, *27*(11), 1388-1411. https://doi.org/10.1002/we.2944

Important note
To cite this publication, please use the final published version (if applicable).
Please check the document version above.

Wind Energy

WILEY

RESEARCH ARTICLE OPEN ACCESS

A Study of the Near Wake Deformation of the X-Rotor Vertical-Axis Wind Turbine With Pitched Blades

David Bensason | Andrea Sciacchitano | Adhyanth Giri Ajay | Carlos Simao Ferreira

Faculty of Aerospace Engineering, Delft University of Technology, Delft, Netherlands

Correspondence: David Bensason (D.Y.bensason@tudelft.nl)

Received: 16 October 2023 | **Revised:** 2 May 2024 | **Accepted:** 2 July 2024

Funding: The authors wish to acknowledge the funding from the European Union's Horizon 2020 research and innovation program under grant agreement No. 101007135.

Keywords: vertical-axis wind turbine | wake re-energization | X-Rotor

ABSTRACT

Recent studies have revealed the large potential of vertical-axis wind turbines (VAWTs) for high-energy-density wind farms due to their favorable wake recovery characteristics. The present study provides an experimental demonstration and proof-of-concept for the wake recovery mechanism of the novel X-Rotor VAWT. The phase-locked flowfield is measured at several streamwise locations along the X-Rotor's wake using stereoscopic particle image velocimetry (PIV) with fixed-pitch offsets applied to the blades. The streamwise vortex system of the upper half of the X-Rotor is first hypothesized and then experimentally verified. The induced wake deformations of the vortex systems are discussed in comparison with previous studies concerning traditional H-type VAWTs. The results suggest that positive blade pitch is more favorable for accelerated wake recovery due to the dominant tip-vortex generated on the upwind windward quadrant of the cycle. Utilizing theoretical blade load variations along the span explains distinct unsteady flow features in the near wake generated at select quadrants of the rotor rotation, shedding light on the potential of the two pitch schemes.

1 | Introduction

Offshore wind energy research and project development is increasing given the favorable wind resource recognized by seaward turbines [1] as well as the attenuation of social acceptance and environmental restrictions for installation [2]. Despite this, the installation and development of offshore wind farms still face several challenges. These include the high levelized cost of energy (LCOE) associated with offshore installations driven by the balance of plant costs [3], which are correlated with the upscaling of turbines and the requirement for strong floating and bottom fixed structures to support the top-heavy designs. Additionally, the availability of economically lucrative offshore resources, fitting the conditions of preferably shallow waters (allowing for cheaper support structures), and proximity to power-demanding coastal regions is limited [4]. As a result, clusters of turbines in wind farms are often placed in close proximity to each other, which in some cases leads to a reduction of performance due to wake losses [5, 6].

Wake losses pose a significant hurdle to farm performance due to the region of low momentum generated directly behind the rotor [6–9]. Wake steering is an extensively studied and applied control strategy for increasing the efficiency of a farm as a whole by decreasing the inter-array wake losses [10, 11]. This technique utilizes a yaw offset of the rotor disk to deflect the wake away from downstream turbines [6, 7, 12]. Although the efficacy of wake steering is very case-specific on a farm's layout and wind resource [13], increases in the total power production of farms have been reported in the range of 4.1%–13% [7, 14].

Vertical-axis wind turbines (VAWTs) have several established advantages over horizontal-axis wind turbines (HAWTs), such as lower levels of sound emissions [15] and independence from wind direction, to name a few [16, 17]. A further advantage in the context of offshore deployment is their lower center of gravity as their heavy instrumentation (gearbox and drive train) can be positioned at the bottom of the tower (or even in the water) [18]. This yields a more stable structure and simplifies the operation and maintenance costs. However, perhaps the most crucial advantage that addresses the hurdle of wake losses and limited offshore space is VAWTs intrinsic ability for an accelerated wake recovery and consequently increased power density of a wind farm [19–22]. This benefit is supported by numerous studies of the wake using lab and full-scale VAWTs [16, 23–25]. These investigations generally credit the counter-rotating streamwise vortices stemming from the blade tips for a high rate of momentum advection in both the near and far wake and, consequently, wake deformation and accelerated recovery with respect to HAWTs [26, 27]. The importance of these flow structures on the complex wake topology is highlighted by the attempts made using simplified objects such as cylinders [28] and mesh disks [29–31], which tend to show discrepancies in the near wake. However, studies have numerically demonstrated that a static actuator cylinder (AC) that mimics the time-averaged three-dimensional loading of a VAWT can accurately model the wake [32, 33]. A recent experimental study by Huang et al. [26] applied the aforementioned 3D AC model on a scaled VAWT geometry, providing an in-depth explanation and experimental demonstration of the trailing vortex system and its impact on wake topology. Further, recent studies [26, 34] have begun to demonstrate promising proposed wake-deflection strategies for VAWTs that utilize blade and strut pitching, which boasts significant gains in performance for closely spaced turbine clusters.

In response to this and the desire to decrease the LCOE of offshore wind and capitalize on the benefits of VAWT technology for high-energy-density wind farms, a novel offshore wind turbine concept known as the "X-Rotor" has been introduced [35], illustrated in Figure 1. The X-Rotor is a radical rethink of the traditional VAWT geometry, which relies on an "aerodynamic gearbox" working principle for electrical power generation. The design includes a coned blade in the shape of an "X," dubbed the primary rotor, accompanied by wingtip-mounted HAWTs, dubbed secondary rotors. A majority of the studies so far have focused on the structural performance of the primary rotor as well as the cost expenditure modeling of the design as a whole [35, 36], yielding results that suggest a potential cost of energy reduction of 20% [35]. A recent study has experimentally investigated the impact of the coned blades on the flow field within the volume of rotation of the primary rotor [37], concluding a potential for the geometry for large-scale farm installation.

The results by Huang et al. [26] showed massive potential for H-type VAWTs for farm installation. Building on the previous experimental investigations around the X-Rotor's [37], the efficacy of fixed pitch settings on the wake control is of particular interest given the X-Rotors design for offshore applications. The present work investigates the impact of fixed blade pitch on the near wake of the primary rotor using phase-locked stereoscopic PIV. Numerical studies [39] have investigated the impact of fixed-blade pitch on the blade loads and performance of

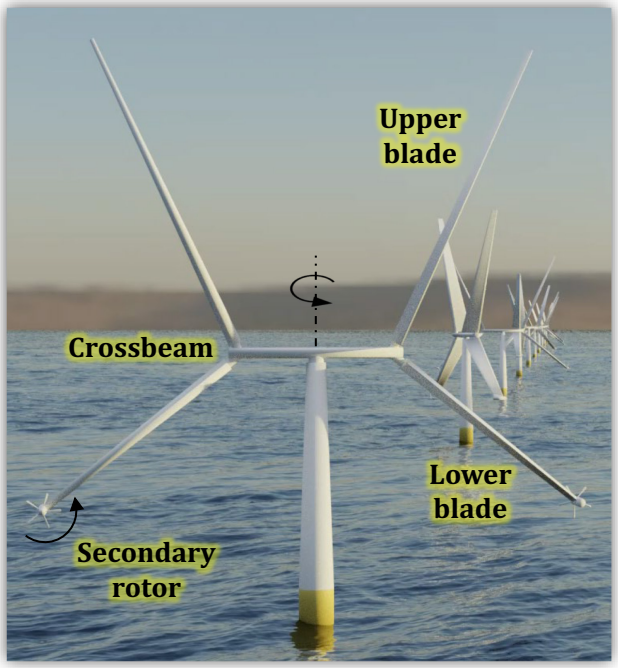

FIGURE 1 | Rendering of the X-Rotor concept adapted from Morgan and Leithead [38]. The primary rotor comprises of the upper and lower blades connected to a crossbeam. The direction of rotation of the primary and secondary rotors is marked.

a full-scale X-Rotor VAWT, demonstrating a penalty in power performance of the primary rotor of up to 20% depending on the tip-speed ratio. However, these studies lacked an analysis of the impacts of this strategy on the wake. The present study focuses on the wake deflection and deformation mechanism imposed by pitched blades while drawing comparisons with previous studies concerning straight-bladed VAWTs. The results confirm the trailing vortex system governs the wake topology. Further, it confirms and demonstrates the potential for fixed blade pitch to modify the rotor loading and, consequently, the vortex system in favor of an accelerated wake recovery for this novel geometry. The remainder of this manuscript is structured as follows. A theoretical analysis of the X-Rotor vortex system is provided in Section 2. A description of the experimental setup and case overview is provided in Section 3. The results and key findings are presented and discussed in Section 4 and followed by a summary and conclusions in Section 5.

2 | Wake Re-Energization Mechanism

The dominant role of streamwise vortices on the wake topology and deflection of a VAWT was experimentally demonstrated by Huang et al. [26]. This phenomenon can be demonstrated by simplifying the loading of a VAWT using the AC approach, as shown numerically by Tavernier et al. [40]. A top-view of the loading on this idealized cylinder is shown in Figure 2. The sectors of the VAWT cycle are upwind windward (UW), upwind leeward (UL), downwind leeward (DL), and downwind windward (DW). The vectors indicate the normal loading direction and magnitude of the blade throughout the cycle. For simplicity, the load is assumed to be uniformly distributed in the upwind and downwind halves

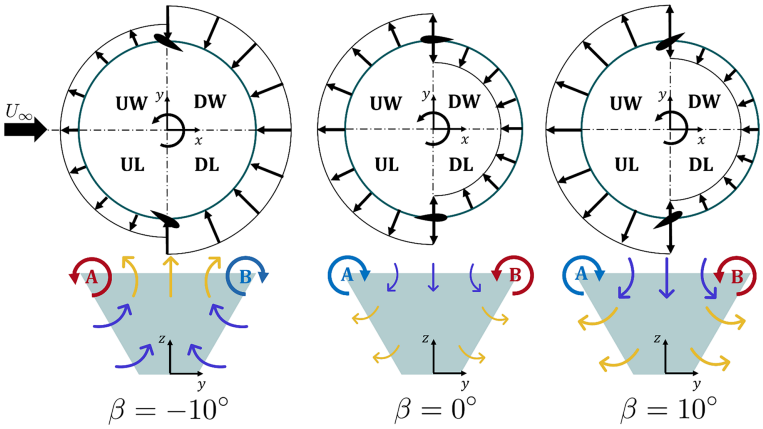

FIGURE 2 | The first row shows a schematic of the simplified force fields over the rotation cylinder of the X-Rotor adopted by Huang et al. [26]. The schematics include blades (exaggerated in size) at azimuths $\theta = 0°$ and 180° for fixed pitch settings $\beta = -10°$, 0°, and 10°, respectively. The curved arrows indicate the anti-clockwise direction of rotation. The second row illustrates the frontal area of the rotor (shaded) along with the dominant streamwise vortices labeled A and B as defined in Figure 3 with the rotation directions when in the inertial frame of reference.

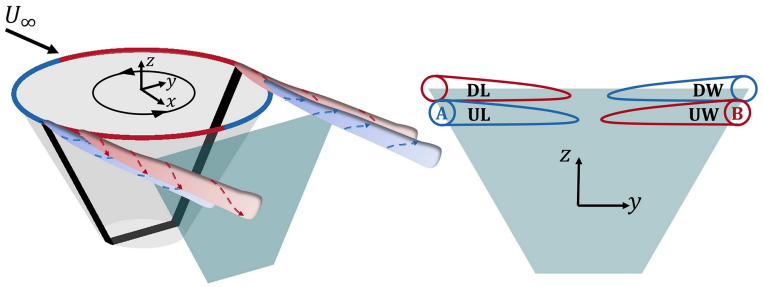

FIGURE 3 | An isometric schematic of the upper half of the X-Rotor at blade pitch $\beta = 0°$. Dominant tip-vortex filaments are color-coded based on the quadrant in which they are generated (blue and red) matching the colored blade tip trajectory. The intersection of these vortical structures on a streamwise plane (shaded) is shown on the right. The vortices are labeled based on the quadrant in which they are generated, where U and D correspond to upwind and downwind, respectively, and W and L correspond to windward and leeward, respectively. The dominant streamwise vortices are labeled A and B for the leeward and windward sides, respectively.

and dominated by the normal load contribution of the blade [40], with the upwind half loaded more heavily for the zero pitch case. A detailed overview of the streamwise vorticity generation as a function of the AC loading is provided by [26]. A representation of the streamwise vortices is shown in Figure 3. The upper half of the X-Rotor VAWT is shown at a phase-locked position of $\theta = 0°$ with a gray shaded cone to represent the actuator surface. The upper tips are shaded red and blue to mark areas where positive ($+\omega_x$, counter-clockwise) and negative ($-\omega_x$, clockwise) streamwise vorticity is generated by the blade, respectively. The generation and shedding of streamwise tip-vortices are an intrinsic feature of VAWT aerodynamics. The tip-vortex strength is proportional to the phase-dependent load of the blade. As this is constantly changing throughout the cycle [41], the circulation of the shed vortex is also continually changing. The direction of rotation of these vortical structures is a function of the loading direction of the blade in the inertial frame of reference and the sign of this bound circulation. This sign flips in the direction at $\theta = 0°$ and 180° as the pressure and suction sides of the blades flip, and at $\theta = 90°$ and 270° [23]. Note that the spanwise vorticity generated by the blade is not presented in this schematic, as it is not a dominant feature in the wake recovery mechanism [30]. Idealized streamwise vortices generated from each AC quadrant are shown with their respective idealized propagation paths shaded. The intersection of these vortices with an arbitrary cross-stream plane (shaded trapezoid section) in the near wake is visualized on the right side of Figure 3 with the quadrants from the AC labeled. The vortices generated in the upwind half of the cycle induce an inboard flow on the upper section of the rotor as opposed to the downwind vortices, which induce an outboard flow. The vortices marked with A and B represent the dominant streamwise vortex in the leeward and windward halves of the rotor, respectively. Consistent with the zero pitch AC shown in Figure 2, these are the vortices generated in the UL and UW quadrants, respectively.

Along with the idealized load distribution of the baseline zero pitch case, the cases for fixed pitch settings of $\beta = -10°$ and $\beta = 10°$ are shown in Figure 2. For the fixed pitch case of $\beta = -10°$, the load on the AC is shifted towards the downstream half of the rotor. This can be attributed to the systematically higher magnitudes in normal loading experience by the blade. As a result of this increased load, the strength of the streamwise vortices increases, consistent with lifting line theory [25]. Following the same reasoning, the positive fixed pitch case of $\beta = 10°$ systematically increases the AC load in the upwind half of the rotor, strengthening the streamwise vortices generated in these respective quadrants.

To understand the impact of these streamwise vortices on the wake topology of the rotor, we assume that the aforementioned structures marked A and B are the dominant sources of induced flow. Hence, although the edges of the rotor wake include counter-rotating vortex pairs (CVPs), it is assumed that the weaker vortices stemming from the less loaded quadrants will merge with the dominant structure. This assumption has been experimentally and numerically validated [26, 40]. These vortices are visualized in Figure 2 on the bottom row when intersecting a cross-stream plane in the near wake of the rotor. Blue and yellow vectors are added to visualize the movement of perturbed flow (wake) and freestream flow, respectively. For the baseline case of $\beta = 0°$, the dominant vortices are those from the UW and UL. These vortices induced a downwash, where freestream flow is injected from above the actuator while the wake is ejected out from the side. The mode of operation is similar for the positive pitch case of $\beta = 10°$ with higher magnitudes in downwash. Finally, the negative pitch case $\beta = -10°$ has dominant vortices stemming from the DL and DW quadrants of the cycle. As a result, free-stream flow is injected from the sides of the rotor while the wake is ejected from the top of the actuator.

For the simplified cases shown in Figure 2, the loads generated in the upwind and downwind halves are perfectly balanced between the leeward and windward sides; as a result, lateral forces generated in the upwind and downwind are null. Hence, there would be no net lateral deflection of the wake, which would deflect symmetrically about the vertical axis. This theory holds for an infinite number of blades [42]. However, in practice, the loads generated in the leeward and windward halves of the rotor are not symmetric in magnitude, and hence, a lateral deflection is also expected [26, 43]. This level of asymmetry increases as the number of blades on the rotor decreases.

3 | Methods

3.1 | Wind Tunnel

Experiments are performed in the Open Jet Facility (OJF) at TU Delft Aerospace Engineering Laboratories, illustrated in Figure 4. The atmospheric closed-loop wind tunnel has an octagonal exit section of 2.85 m × 2.85 m with a contraction ratio

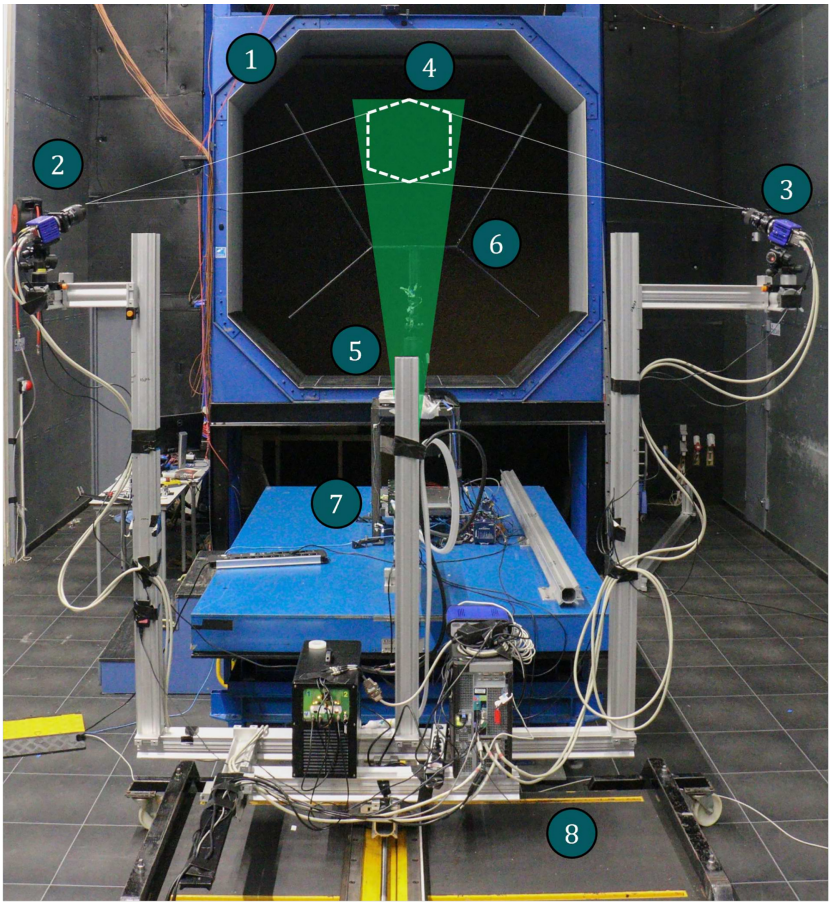

FIGURE 4 | Experimental setup in the OJF. A visualization of the measurement plane is provided (green cone) along with labeled key components of the measurement system.

of 3:1. A controlled streamwise velocity of $U_\infty = 4\,\mathrm{m\,s^{-1}}$ is used throughout the experiment. The resulting jet stream is bound by shear layers with a semi-angle of 4.7° with turbulence intensities reported to be 0.5% within the testing region [44].

3.2 | Scaled X-Rotor Model

A 1:100 scale X-Rotor model is mounted in the center of the test section, as illustrated in Figure 4. The model consists of four straight NACA0021 airfoils with a constant chord of $c = 0.075\,\mathrm{m}$ attached to a stiff crossbeam with the same profile and chord and length of 0.5 m. The top and bottom blades have a tip diameter of $D = 1.5\,\mathrm{m}$ and coning angles of 60° and 40°, respectively. The upper and lower blade lengths are 1 and 0.65 m, respectively. The rotor is supported via a tower with a diameter of 0.06 m. The model is mounted on a base frame with instrumentation such as a motor, rotary encoder, torque sensor, and load cells. A detailed overview of the instrumentation is provided by LeBlanc et al. [45].

3.3 | Flow Measurement System

A stereoscopic particle image velocimetry (PIV) system is used to measure several velocity fields at discrete cross-stream locations in the wake of the X-Rotor. Seeding is generated via a SAFEX smoke generator with an average particle diameter of 1 µm and particle density $10^3\,\mathrm{kg\,m^{-3}}$. The particles are illuminated with a Quantel Evergreen double-pulsed Nd:YAG laser with a sheet thickness of approximately 4 mm. Dual pulses with a wavelength of 532 nm and 200 mJ of energy are generated. Finally, images are captured at a frequency of 15 Hz using two LaVision sCMOS cameras shooting from opposing sides of the laser sheet. With a focal length of 105 mm, numerical aperture 8, and stereoscopic angle of 74.8° between cameras, the resulting field of view (FOV) is approximately 43 cm × 30 cm, yielding a digital image resolution of 6 px/mm. A time of 320 µs between images is used. Based on the numerical aperture of the lenses and the image magnification M = 0.01, the diffraction diameter of the particle images can be calculated using Equation (1) as 10.3 µm. This is 1.5 times the pixel size (6.6 µm), resulting in limited peak locking errors [46].

$$d_{\mathrm{diff}} = 2.44 \times f_{\#} \times (M+1) \times \lambda \tag{1}$$

The resulting images are processed with a cross-correlation-based image interrogation algorithm with window deformation, with window sizes of 256 px × 256 px and 96 px × 96 px and an overlap factor of 75%. A total of 120 vector field images were captured for each measurement plane and phase averaged. The camera and laser systems are rigidly connected and mounted on a traversing system, enabling a translation range in the streamwise and lateral direction of 1.5 and 0.5 m, respectively.

3.4 | Case Overview

The aforementioned measurement system captures phase-locked measurements of the flowfield across cross-stream locations in the X-Rotor's wake, as visualized in Figure 5. The origin of the coordinate system is taken as the center of the crossbeam, with the y and z defined as the lateral and axial directions, respectively.The cross-stream planes measured range from distances of 0.39–2.4 m from the crossbeam center, corresponding to normalized distances of $x/D = 0.26$ and 1.6, respectively. The measurements from the three cross-stream planes $x/D = 0.26$, 0.90, and 1.6 are predominantly used in Section 4. However, an extended set of cross-stream planes was measured, with a complete overview provided in Appendix B. At a given cross-stream location, several planes are measured in the y-axis and z-axis directions via the traversing system described in Section 3.3 and stitched together when post-processing the results. Three fixed pitch settings were tested, namely, $\beta = 10°$ (pitched in), $\beta = -10°$ (pitched out), and $\beta = 0°$ (baseline). These fixed pitch settings were realized by modifying the blade connection point to the crossbeam. The wake is measured at a constant rotor rotational frequency of $\omega = 21.3\,\mathrm{rad/s}$, corresponding to a tip-speed ratio $\lambda = \omega R/U_\infty$ of 4 and chord-based Reynolds number of $\mathrm{Re_c} = 8.1 \times 10^4$. Due to time constraints, the measurement focuses on the wake

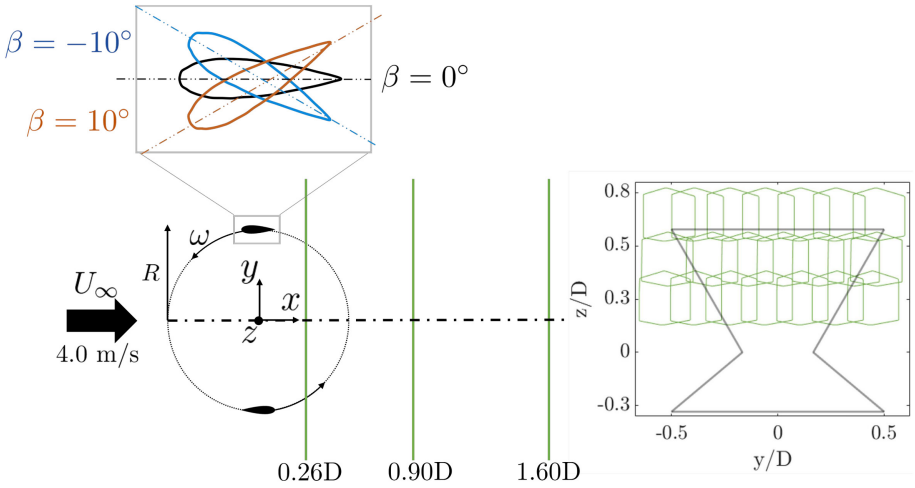

FIGURE 5 | Schematic of the top view of the setup (left). Enlarged blades are shown at azimuths $\theta = 0°$ and 180° with primary measurement planes (green) for the subsequent analysis marked. A magnified view of the blade orientation at fixed pitch settings $\beta = -10°$ (blue) and $\beta = 10$ ° (brown) is provided. Frontal view of the measurements planes (right) for the example of $x/D = 0.9$ and pitch $\beta = 10°$.

behind the upper blades of the X-Rotor, spanning from $z/D =$ 0.15 to 0.8 for the pitched cases $\beta = 0°$ and 10°, and $z/D = 0.35$ to 0.8 for the pitch case $\beta = -10°$.

3.5 | Numerical Demonstration of Rotor Load Distribution

As explained in Section 3.2, load cells at the base of the rotor are used to measure the streamwise and lateral thrust components of the rotor over its rotation. However, this does not yield blade-level loading nor an integrated load for each blade. Hence, to support the arguments made in this work, simulations of the scaled X-Rotor model were run using the vortex lattice approach of the Code for Axial and Cross-flow Turbine Simulation (CACTUS) [47]. The upper blades of the X-Rotor are discretized into 18-blade sections and run for 13 revolutions to attain convergence with a second-order predictor time advancement scheme. The simulated load data of the final revolution is used in the subsequent discussion. The crossbeam and tower were not modeled in this numerical setup. A freestream flow of $U_\infty = 4\,\mathrm{m\,s^{-1}}$ is used for the simulation, with an XFOIL [48] statically simulated polar for a NACA0021 blade at Reynolds number 15×10^4.

The numerical results of the effective angles of attack of the top blades at each spanwise location and rotor azimuth are shown in Figure 6 for each of the fixed pitch cases. The quadrants as defined in Figure 2 are labeled along with a black contour line indicating the static stall angle of the NACA0021 blade. In this case, the static stall angle is simulated to be $\alpha_{ss} = 9.1°$.

For the baseline pitch case of $\beta = 0°$, the region in which the stall angle gradually narrows in the upwind half of the cycle towards the tip of the upper blade. Below this, the blade experiences a large stall in the UL quadrant, initiated towards the end of the UW quarter. In the downwind half of the cycles, the flow remains attached for a larger section of the span while experiencing stall on the lower 60% of the span up to an azimuth of approximately $\theta = 330°$. Consistent with the description in Section 2, a negative pitch offset ($\beta = -10°$) to the blade reduces the angles of attack experienced in the upwind half of the rotor significantly and, consequently, reduces the loads of the blades. However, the magnitudes in the angle of attack are increased drastically in the downwind half. As a result, the blade is stalled for a majority of this half of the cycle, with sections falling within the stall limit for the upper sections of the span. Similarly, the positive pitch case ($\beta = 10°$) systematically lowers the angles of attack experienced by the blade in the downwind half of the cycle, with a very small region of spans falling within the stall limit. However, the angles surpass the stall limit in the upwind half of the rotor across all spanwise locations, starting at an azimuth of approximately $\theta = 16°$.

Although large regions of separated flow across all pitch cases for span-wise locations near the root section are evident, the most significant contribution of aerodynamic load stems from the regions closer to the tip. Hence, to further understand the impact of blade pitch as a function of rotor azimuth for the blade as a whole, the blade integrated normal load is shown in Figure 7 for each fixed pitch case. The blade integrated loads C_N are shown similarly to Figure 2. Furthermore, the percentage difference with respect to the pitch case of $\beta = 0°$ for the integrated load over the area of each quadrant is shown for the positive and negative pitch cases. The numbers are color-coded, with green and red signifying an increase and decrease, respectively.

Consistent with the angle of attack magnitudes in Figure 6 and the discussion in Section 2, the loading of the X-Rotor is higher in the upwind half for the baseline pitch case of $\beta = 0°$. As mentioned in Section 2, the symmetric loading between the windward and leeward halves of the rotor is a simplification of the system. In reality, the loading in the windward half of the rotor is higher due to the asymmetric angle of attack variation and induction of the rotor, highlighted in Figure 6. For the positive pitch case $\beta = 10°$ the normal load of the blade increases in the upwind half of the cycle, most significantly in the UW quadrant. Consequently, the load decreases in the downwind half of the cycle, consistent with Figure 6. Finally, the negative pitch case increases the normal loading of the blade in the downwind half of the rotor while reducing that in the upwind half. Not only does the action of pitching the blades alter the magnitudes of blade loading in the respective quadrants, but also the percentage of time spent in each quadrant with positive and negative normal loads. In the inertial frame of reference, depending on if the blade is in the windward or leeward half of the cycle, the normal load direction governs the direction of vorticity generated at the tip, described in Section 2. For the negative fixed pitch case, the blade experiences a negative load

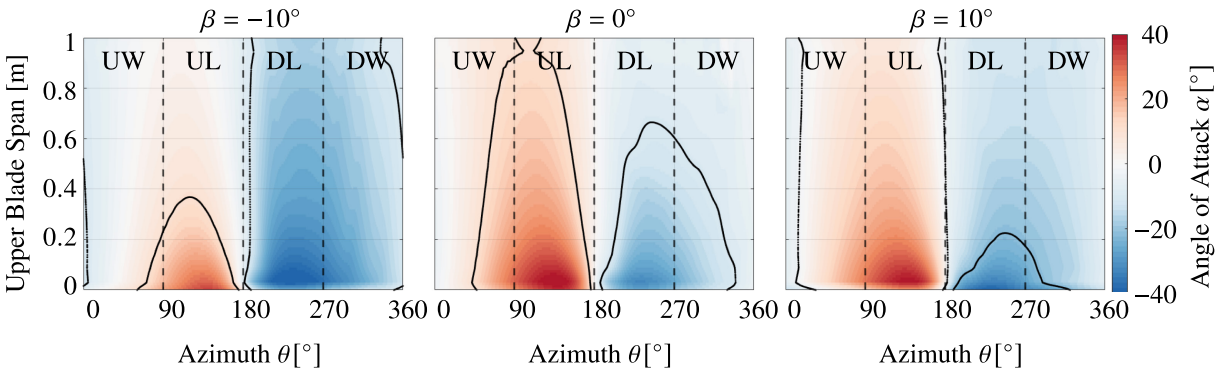

FIGURE 6 | Effective angle of attack α of the top blades as a function of azimuth locations θ and normalized blade span position for each fixed pitch case. The black contour line indicates the static stall angle of the NACA0021 airfoil of $\alpha_{ss} = 9.1°$. Vertical dashed lines separate the different quadrants of the rotor as described in Figure 2.

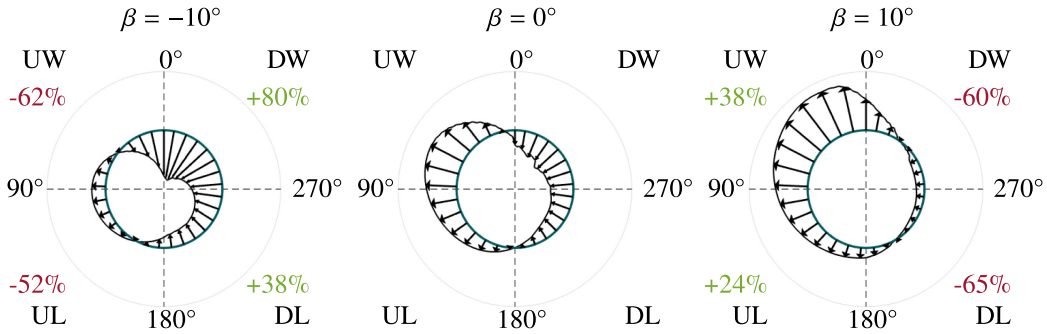

FIGURE 7 | Numerical results of the blade integrated normal load C_N as a function of blade azimuth for each fixed pitch case. The solid circular line indicates the case where the normal load is zero. Flow comes from left to right. The percentage differences for each quadrant with respect to the zero pitch case $\beta = 0°$ for the fixed pitch offsets are shown, with red and green signifying a decrease and increase, respectively.

coefficient (inward) for a larger percentage of the cycle in both the leeward and windward halves of the cycle compared to the zero pitch case. This confirms the dominance of the streamwise CVP generated in the download half of the cycle, as highlighted in Figure 2. Similarly, the positive pitch case increases the percentage of time the blade experiences a positive (outward) normal load in both the windward and leeward halves of the cycle, ascertaining the dominance of the upwind-generated vortices. Similar behavior was experimentally observed by LeBlanc and Ferreira [43] for a straight-bladed VAWT model.

3.6 | Uncertainty in Flowfield Analysis

Given the relatively high complexity of the flow measurement system, we aim to quantify certain sources of uncertainty in the flow measurements. Following the work of Sciacchitano and Scarano [49] and Huang et al. [26], the standard uncertainty of the phase-locked velocity field can be calculated as

$$U_{U*} = \frac{k\sigma_{U*}}{\sqrt{N}} \tag{2}$$

where σ_{U*} is the standard deviation of the average phase-locked velocity components U_x, U_y, and U_z over N images. The ratio is multiplied by a coverage factor $k = 1.96$ to expand the standard uncertainty to a 95% confidence interval. As described in Section 3.3, the number of images collected for each FOV is $N = 120$. For the streamwise flow component, the highest magnitude in σ_{U*} is for the $\beta = 0°$ case is $1.2\,\mathrm{m\,s^{-1}}$, resulting in a standard uncertainty of $U_{U_x*} = 0.21\,\mathrm{m\,s^{-1}}$. Following the same procedure, the maximum standard uncertainties in the lateral and axial directions are $U_{U_y*} = U_{U_z*} = 0.18\,\mathrm{m\,s^{-1}}$, respectively. These relatively high standard deviations are attributed to large regions of separated flow in the near wake of the X-Rotor due to the coned nature of the blades, as further described in Sections 3.5 and 4.4. When considering regions of the wake outside these regions, the σ_{U*} are the order of magnitude of $0.12\,\mathrm{m\,s^{-1}}$ for the three flow components, resulting in $U_{U_x*} = 0.02\,\mathrm{m\,s^{-1}}$.

In addition to the standard uncertainty of the phase-locked flow components, the standard uncertainty of the phase-locked streamwise vorticity component U_{ω_x} is calculated as

$$U_{\omega_x} = \frac{U_{U*}}{d}\sqrt{1 - \rho(2d)} \tag{3}$$

where U_{U*} is the standard uncertainty in the axial (U_{U_z*}) or lateral (U_{U_y*}) direction [50]. The grid spacing of the integration window is denoted as d, and the cross-correlation coefficient of the spatially correlated velocities is denoted as $\rho(2d)$. Given a camera scaling factor of 7.27 px/mm and correlation window size of 96 px × 96 px, the dimensional grid spacing is calculated as $d = 13.2\,\mathrm{mm}$. The cross-correlation coefficient adopted for this work is $\rho(2d) \approx 0.45$ [50], yielding a standard uncertainty in the streamwise vorticity in the regions of separated flow as $U_{\omega_x} = 10.1\,\mathrm{s^{-1}}$. When adopting the standard uncertainty in the velocity outside this region, the value is computed as $U_{\omega_x} = 1.1\,\mathrm{s^{-1}}$.

A further source of uncertainty when dealing with phase-locked measurements is phase unsteadiness in the system. This can be attributed to either vibration in the measurement system or errors in the time delay for the triggering of the cameras and laser system. When the wake has low magnitudes in velocity and gradients, the unsteadiness in the system will have a minimal impact on the average value. However, in cases where there are large flow gradients, such as regions near the tip-vortex of the rotor, the impacts of this unsteadiness can be larger on the computed average.

The percentage error in the velocity magnitude $|U|$ with respect to the mean value $|U_{120}|$ is shown in Figure 8. Rather than showing the convergence over the entire range, the analysis is performed for two subsets of $N = 60$ cycles. The convergence of randomized acquisitions are denoted as $|U_{1-60}|$ and $|U_{61-120}|$ for the two subsets, respectively. The convergence is tested for two representative cases where we expected lower and higher gradients. For the low gradient representative case, the convergence at the center of the wake with pitch $\beta = 0°$ at $x/D = 0.26$ is shown, as illustrated by the subfigure in Figure 8. The curves for both subsets of acquisitions fall consistently below a 1% difference with respect to the average over the full range of acquisitions $|U_{120}|$. For the high gradient representative case, the the convergence near the windward vortex for a pitch case $\beta = 10°$ at $x/D = 0.4$ is shown. The difference with respect to the mean of the full range is higher compared to the $\beta = 0°$ case for both subsets of acquisitions. Both fall within a 1% difference beyond a sample size of $N = 20$. The percentage difference ϵ

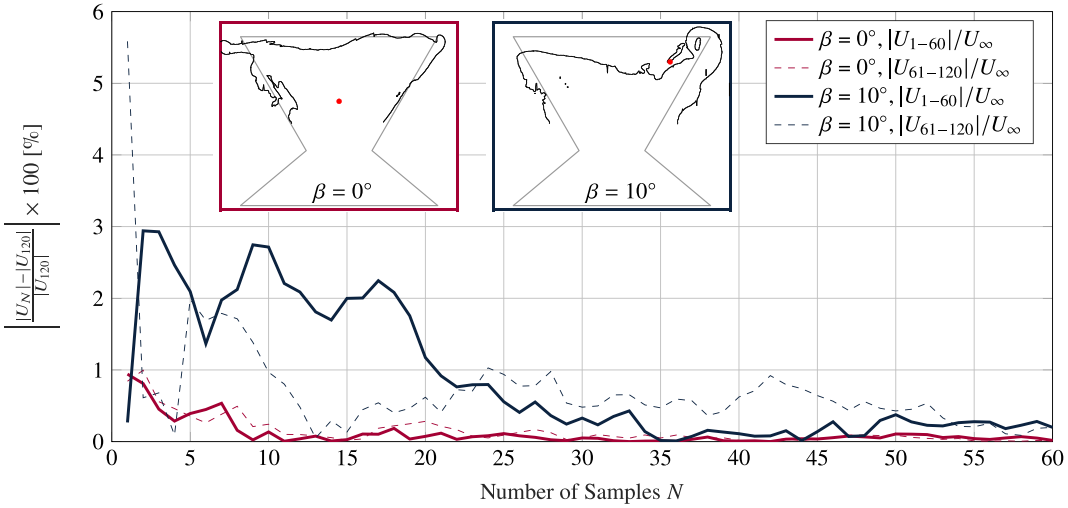

FIGURE 8 | Statistical convergence of the difference in phase-locked velocity magnitude $|U|$ with respect to the average over $N = 120$ acquisitions $|U_{120}|$ for subsets 60 data acquisitions. The convergence of a case near the center of the wake for pitch case $\beta = 0°$ at $x/D = 0.26$ is shown in red and that for $\beta = 10°$ at $x/D = 0.4$ is shown in blue. The respective color-coded wake shapes for the two cases are shown with red dots indicating the point for which the convergence is presented.

between the converged subsets of values for the two pitch cases are computed as follows:

$$\epsilon = \frac{\left||U_{1-60}| - |U_{61-120}|\right|}{\frac{|U_{1-60}| + |U_{61-120}|}{2}} \times 100 \tag{4}$$

Using the final converged values for the subsets, the percentage difference for the pitch cases $\beta = 0°$ and 10° are computed as 0.03% and 0.40%, respectively. This analysis has been performed for several other locations in the wake across all pitch cases to confirm a converged data set.

Finally, uncertainty associated with the traversing and subsequent stitching of measurement planes is addressed. As described in Section 3.4, a traversing system is used to acquire several measurement planes at a given streamwise location before being stitched together when post-processing the results. Uncertainties in this process may arise in the stitching from random and human errors in the traversing system operation as well as the accuracy of the system itself. The root-mean-square error (RMSE) for the velocity magnitudes is computed for the overlapping regions of planes as follows:

$$\text{RMSE} = \sqrt{\frac{\sum_{i=1}^{N} (|U_{1,i}| - |U_{2,i}|)^2}{N}} \tag{5}$$

where $|U_1|$ and $|U_2|$ are velocity magnitude values at a given index i in an overlapping regions between two planes and N is the number of overlapping indices. The RMSE for overlapping acquisitions in the same regions as discussed with Figure 8 are computed as 0.23 m s^{-1} and 0.13 m s^{-1} for the pitch cases $\beta = 0°$ and 10°, respectively. Once again, the same analysis was conducted for overlapping acquisitions at different locations in the wake of all pitch cases to ensure the accuracy of the stitching process.

4 | Results

4.1 | Velocity Fields

The phase-locked streamwise, lateral, and axial velocity contours are shown in Figures 9–11 for each of the fixed pitch cases at cross-stream locations $x/D = 0.26$, 0.90, and 1.60. All velocities are normalized by the free stream velocity U_∞ with a black contour of the wake at $U_x/U_\infty = 0.9$. The frontal area of the rotor at an azimuth of $\theta = 0°$ is shown via a gray line with quivers showing the in-plane velocities in black. An extended set of measurements at more cross-stream planes is shown in Appendix B.

The measurements do not extend towards the upper blades' roots, so the pitch case's wake $\beta = -10°$ does not display streamwise flow deficits below $0.6U_\infty$. The wake shape shows an elongation in the axial direction that extends when moving along in the streamwise direction, with a more pronounced extension on the windward half of the rotor. This axial stretching of the wake is confirmed by the strong presence of axial flow U_z in the upper section of the wake, shown in Figure 11. In addition to the axial expansion, a radial contraction is also evident on the leeward side of the rotor, shown in Figure 10. This is consistent with the strong positive radial flow of $0.3U_\infty$ in the leeward half of the rotor throughout the wake. This is complemented further by the negative radial flow components on the windward side of the rotor.

The measurements for the pitch case $\beta = 0°$ extend further towards the roots of the upper blades and feature higher streamwise flow deficits of up to $0.3U_\infty$ than the aforementioned case. Minimal expansion has occurred in the near-wake region; hence, the wake profile follows the coned shape of the rotor. Similar to results reported by Tescione et al. [23], a difference in the flow deficits between the windward and leeward halves of the rotor is visible due to the asymmetric loading of the rotor, which is further highlighted by heavier radial wake extension on the windward side of the rotor. This asymmetry

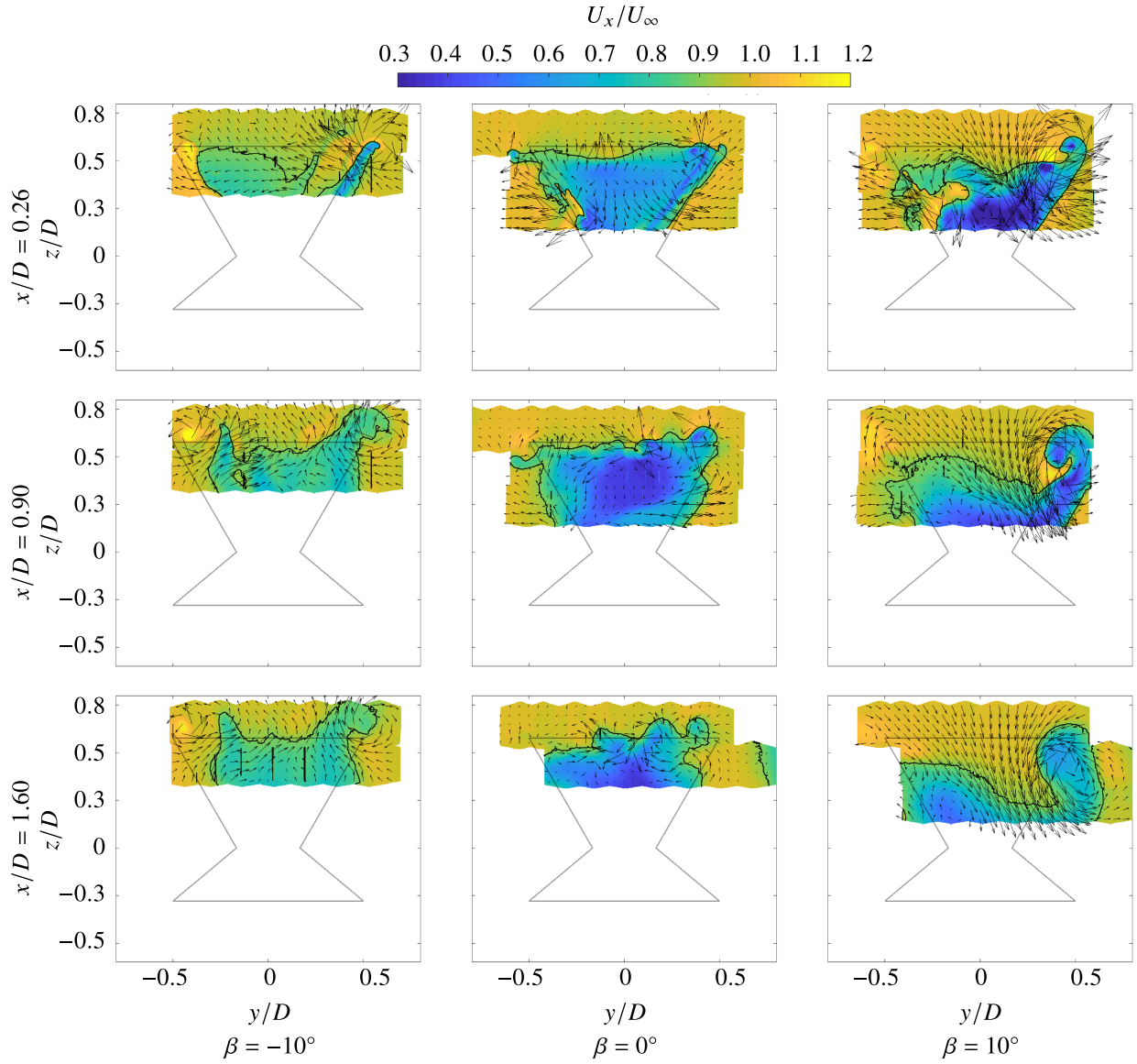

FIGURE 9 | Normalized streamwise flow (U_x/U_∞) at cross-stream locations $x/D = 0.26$, 0.90, and 1.60 for fixed pitch cases $\beta = -10°$, 0°, and 10°. The gray solid line shows the frontal area of the rotor at an azimuth of 0° with a black contour line showing where $U_x/U_\infty = 0.9$. Quivers show the in-plane velocity vectors.

has also been observed by Huang et al. [26] and can be further justified by the vorticity distributions in the wake, discussed in Section 4.2. Unlike the negative pitch case, there is minimal axial flow with magnitudes around $0.1U_\infty$ in areas distant from tip-vortices. A change in magnitude and location of local upwash and downwash in the near wake across the cross-stream locations is evident. This is due to the coherent shed and tip vortical structures within the rotation volume in the rotor having periodic induced velocities. The radial flow suggests a general wake expansion with positive and negative magnitudes of U_y on the windward and leeward sides of the rotor, respectively.

Finally, the positive pitch case $\beta = 10°$ shows a significant radial deflection of the wake towards the windward side of the rotor, similar to the results reported by Huang et al. [26] for straight-bladed VAWTs. The positive pitch case features a more significant flow deficit than the aforementioned cases directly behind the rotor. This can be attributed to the higher lift generated by the advancing blades on the windward side of the rotor. This further translates to an increased lateral force induced on the flow, as confirmed by Figure 10, leading to a wake expansion radially outward on the windward side. Starkly different from the negative pitch case, the wake shape suggested an axial contraction that extends in the streamwise direction. This is concentrated mainly on the windward half of the rotor and is visible via the large vertical downwash on the order of $0.3U_\infty$ shown in Figure 11. This is accompanied by a strong presence of positive radial flow on the windward side and negative on the leeward.

4.2 | Verification of the Vorticity System

The measured streamwise vorticity at cross-stream locations $x/D = 0.26$, 0.90, and 1.60 is shown in Figure 12 for the fixed

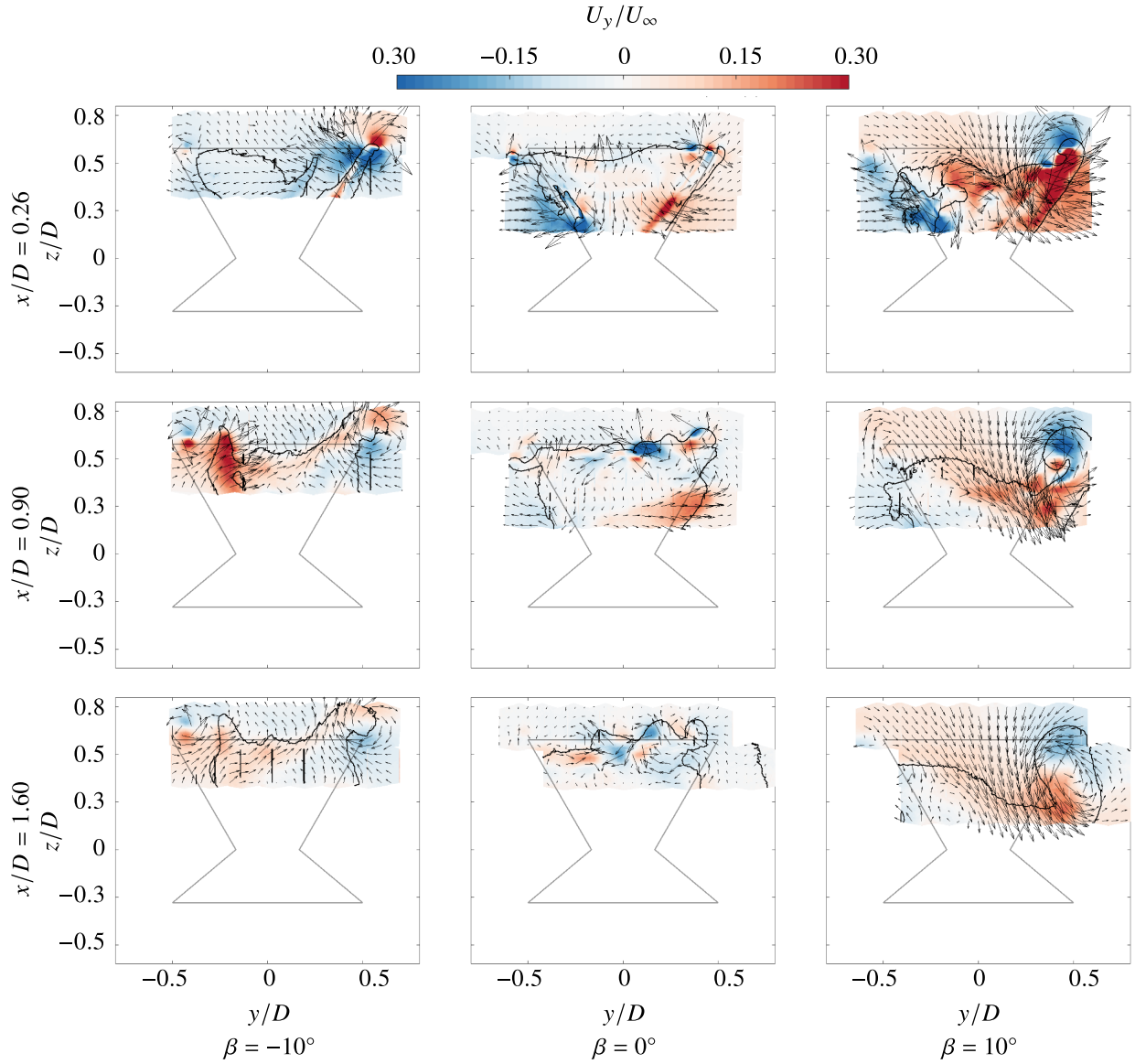

FIGURE 10 | Normalized streamwise flow (U_y/U_∞) at cross-stream locations $x/D = 0.26$, 0.90, and 1.60 for fixed pitch cases $\beta = -10°$, 0°, and 10°. The gray solid line shows the frontal area of the rotor at an azimuth of 0° with a black contour line showing where $U_x/U_\infty = 0.9$. Quivers show the in-plane velocity vectors.

pitch cases $\beta = -10°$, 0°, and 10°. In-plane velocity vectors are illustrated to help locate the vortical structures labeled based on the convention proposed in Section 2. The black contour line indicates where $U_x/U_\infty = 0.9$, and the gray enclosed curve indicates the frontal area of the rotor. An extended set of measurements at more cross-stream planes is shown in Appendix B.

For all pitch cases, the vortical structures are clearly present at the $x/D = 0.26$. As this plane is still within the volume of rotation, the presence of shed vorticity of the blade is visible, specifically for the $\beta = -10°$ and 10° cases. For the pitch cases $\beta = 10°$, the vortex generated in the UW quadrant (B) creates a dominant downwash of the wake, contracting the wake perimeter to within the frontal area of the rotor. Due to the high strength of this vortex, that of the previous blade is also visible, which has convected downstream. The UL vortex (A) is also present but visibly weaker and hence induces a similar axial contraction of the wake on the leeward side of the rotor but to a lesser degree. The negative pitch case $\beta = -10°$ exhibits a similar CVP with opposite direction to the aforementioned case as predicted in Section 2. The vortices generated in the DW (B) and DL (A) quadrants are dominant and induce an axial expansion of the wake. Once again, the windward vortex is seemingly stronger in magnitude. The upwind vortex, albeit weaker, has convected inward towards $y/D = 0$ and includes a regional upwash of the wake. Finally, the case with no pitch $\beta = 0°$ exhibits three vortical structures towards the windward side of the rotor with alternating rotation direction. As this plane is still within the volume of rotation and these are phase-locked measurements, the tip-vortices of the passing and previously passed blade are visible. In this case, the DW-generated vortex (B) stems from the blade, which has just passed and is now at phase-locked position $\theta = 0°$. The surrounding vortex pairs (B) were generated in the UW quadrant by the two blades in the previous cycles that have convected downstream.

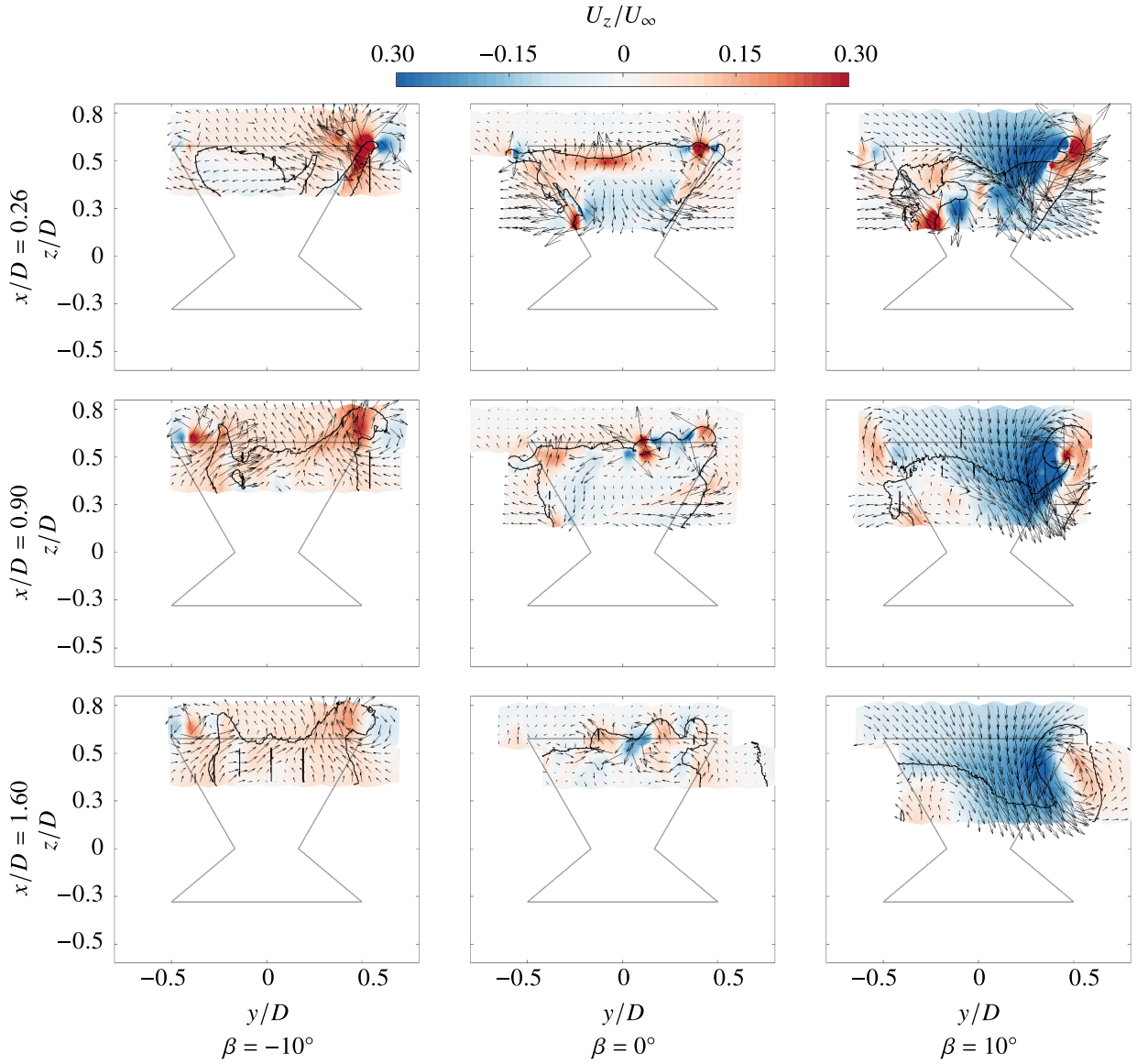

FIGURE 11 | Normalized streamwise flow (U_z/U_∞) at cross-stream locations $x/D = 0.26$, 0.90, and 1.60 for fixed pitch cases $\beta = -10°$, 0°, and 10°. The gray solid line shows the frontal area of the rotor at an azimuth of 0° with a black contour line showing where $U_x/U_\infty = 0.9$. Quivers show the in-plane velocity vectors.

The impact of the vortex system on the wake increases in the next cross-stream plane $x/D = 0.90$. For the case of $\beta = 10°$ the size of the UW vortex (B) has grown and convected slightly downward towards $z/D = 0$. The surrounding shed vorticity of the blade has dissipated as we exit the volume of rotation of the rotor. The induced downwash of the vortex has increased due to the larger size of the structure, causing a larger degree of wake deformation and region of high-speed flow within the frontal area of the rotor. The UL vortex (A) is not labeled at this cross-stream location, as it has seemingly diffused. However, its impact on the wake is still present at this location, with a slight axial contraction on the leeward side of the rotor. For the pitch case $\beta = -10°$, the DW vortex (B) has diffused and convected upward above the AC surface. In contrast, the DL vortex (A) has increased in strength while continuing to induce a strong axial contraction of the wake. The zero pitch case $\beta = 0°$ once again exhibits two tip-vortices generated in the UW quadrant (B) of the cycle, which have convected downstream, as well as the vortex generated in the DW quadrant (A) of the blade which has just passed.

Finally, the most downstream plane $x/D = 1.60$ suggests that the vortical structures across all pitch cases are still present but have diffused and mixed substantially. For the positive pitch case $\beta = 10°$, the UW vortex (B) has diffused to a degree where no clear core is identifiable. However, the structure continues to induce a local downwash on the windward side of the rotor, with freestream flow being injected from the upper surface of the AC. Little difference in the wake structure on the leeward side of the rotor is notable compared to the previous cross-stream location presented. The negative pitch case $\beta = -10°$ still displays two coherent vortex structures, which have both convected above the actuator surface. The zero pitch case $\beta = 0°$ shows no coherent vortex structures due to the mixing process of the closely spaced CVP in the near wake. This mixing and turbulent diffusion is intrinsic to VAWTs [23, 37]. The outward motion (above

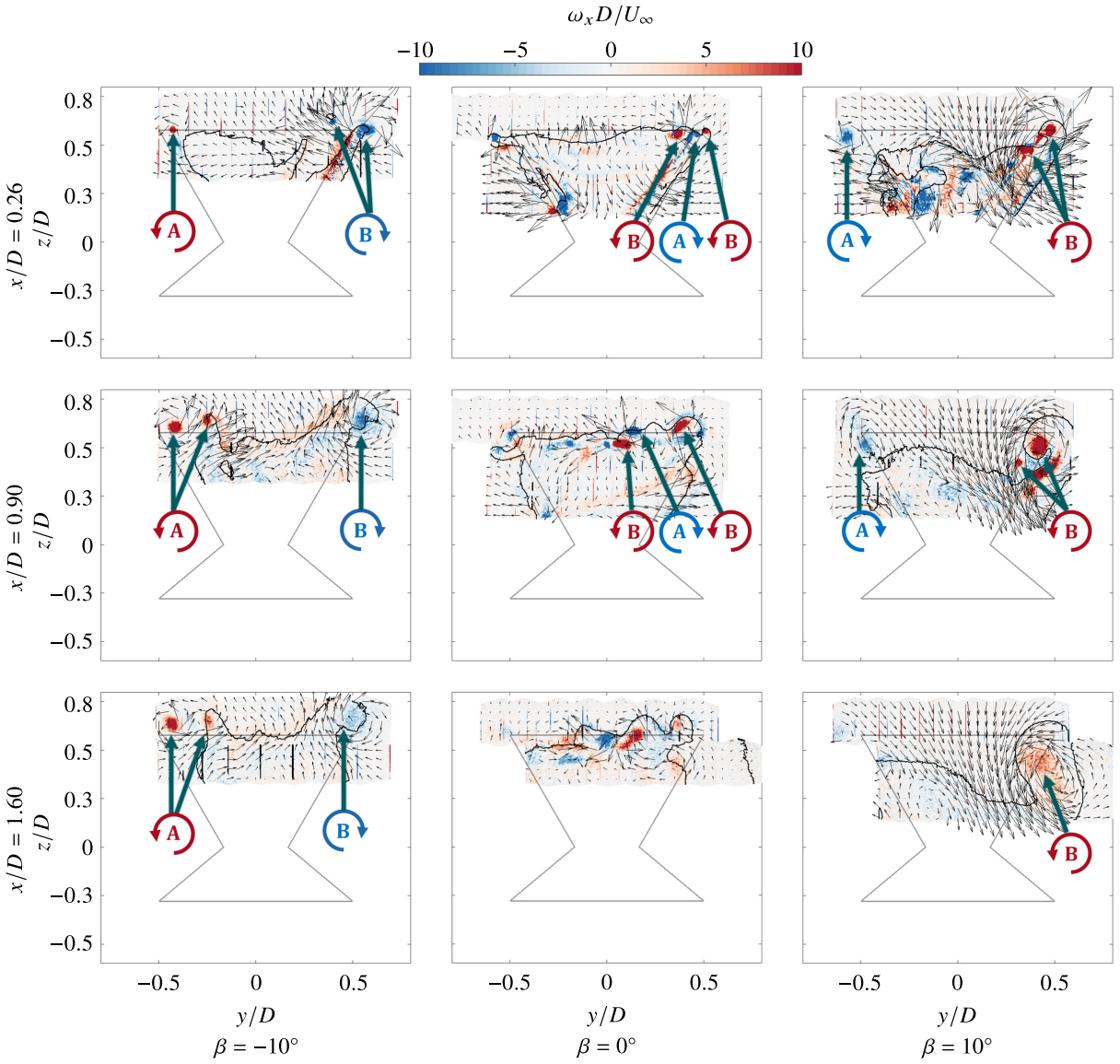

FIGURE 12 | Streamwise vorticity contours at cross-stream locations x/D = 0.26,0.90, and 1.60 for fixed pitch cases $\beta = -10°$, 0°, and 10°. Vortices are labeled for clarity corresponding to markings presented in Figure 2. The black contour line indicates where $U_x/U_\infty = 0.90$. The gray line represents the frontal area of the rotor.

the AC surface) of the vortex structures generated on the windward side of the rotor has been observed experimentally [23, 37] and numerically [51] and can be attributed to the interaction of the tip-vortices of the blade in quadrant UW and the second blade generated in the DW quadrant.

To further highlight the relative impact of blade pitching on the strengths of the tip-vortices, Figure 13 shows the maximum streamwise vorticity strengths $max(\omega_x)$ of the vortices in the windward (W) and leeward (L) halves of the rotor as a function of the cross-stream location. The maximum vorticity is normalized by the highest vortex recorded, which is that of the positive pitch case on the windward side $max(\omega_{x,+10})$ at $x/D = 0.26$.

Across all cases, the maximum vorticity magnitude tends to decrease when moving further downstream in the wake. This is consistent with the observations made of Figure 12 and can be attributed to the mixing and diffusion process of the tip-vortex structures. A deviation from this trend is evident at $x/D = 0.5$ for the vortex of the negative pitch case on the leeward side, where there is an increase in strength from the previous plane. As explained in Section 2, negative blade pitch causes greater loads to be applied to the downwind half of the rotor. Hence, the generation of a strong tip-vortex occurred in the DL quadrant of the cycle and has a delayed appearance in the flowfield compared to the heavily loaded upwind case of the positive pitch. The peak vorticity at the most upstream plane $x/D = 0.26$ corresponds to the vortex generated in the UL quadrant of the cycle, and that at $x/D = 0.5$ in the DL quadrant, as labeled in Figure 12.

The maximum vorticity strengths on the leeward side of the rotor for the positive pitch case remain low in magnitude across all streamwise planes. As described in Section 2, positively pitching the blade increases the blade loading in the upwind half of the rotor with an increase in relative angle of attack across the span. As shown in Figure 6, the angles of attack eventually

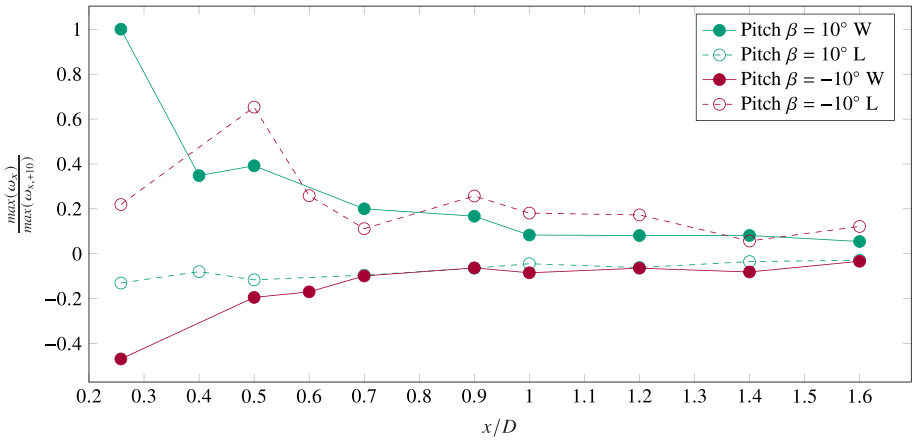

FIGURE 13 | Maximum streamwise vorticity $max(\omega_x)$ strength as a function of cross-stream location for the positive and negative pitch cases. Solid lines indicate vortices on the windward side (W) and dashed on the leeward (L). Values are normalized by the maximum vorticity of the inward vortex in the positive pitch case at $x/D = 0.26$ ($max\,(\omega_{x,+10})$).

exceed the stall angle towards the end of the UW quadrant of the cycle. Hence, the blade is stalled for a large portion of the cycle's UL quadrant, leading to a weaker tip-vortex structure. A similar phenomenon occurs for the negative pitch case in the DW quadrant of the cycle. With the higher angle of attack magnitudes in the downwind half of the rotor, the blade stalls in the DL quadrant of the cycle, leading to a separated flow majority in DW quadrant of the cycle and, hence, a weaker tip-vortex structure.

4.3 | Rotor Induction

The proposed vortex system was verified in Section 4.2. The subsequent impacts of these structures on the distribution of streamwise flow deficits ($(U_x - U_\infty)/U_\infty$) are presented more clearly in Figure 14 for the wake positions of $x/D = 0.26$, 0.90, and 1.60 for the three pitch cases. The frontal area of the rotor is represented with a gray line.

For the baseline case of zero pitch $\beta = 0°$, the region of flow deficit remains within the frontal area of the rotor for the most part as we are in the near wake, and minimal expansion has occurred. At the cross-stream location $x/D = 0.9$ the wake has expanded beyond the frontal area of the rotor both laterally and axially due to the average expansion of the wake. At the most downstream location $x/D = 1.60$ the wake has convected above the actuator surface on the windward side of the rotor, consistent with the vortex system discussed in Section 4.2.

For the positive pitch case $\beta = 10°$ an immediate effect at $x/D = 0.26$ of the dominant vortical structure in the UW quadrant is visible on the windward half of the rotor, with the flow deficit of the wake contracted below the frontal area of the rotor. This axial contracting is complemented by a lateral expansion, with regions of flow deficit evident outside the frontal area of the rotor on both the windward and leeward halves of the rotor. A notable region of flow acceleration is evident on the windward half of the rotor due to the convection of the tip vortex from a previous blade passage. As these results are phase-locked and still in the near wake of the rotor, the coherent tip-vortices from previous cycles intersect the measurement plane at instances where the vortex tube is not perfectly perpendicular to the plane [37]. Hence, the out-of-plane flow acceleration on the upper part of the vortex is captured and evident in regions of dominant vortical structures. A similar structure is evident on the leeward side of the rotor as well due to the acceleration of flow over the large-scale vortex generated in the UL quadrant of the cycle. At the cross-stream location $x/D = 0.90$ the wake has ejected further out laterally while contracting even further in the axial direction. The flow deficit stemming from the large-scale vortex has grown in size, consistent with the observations in Section 4.2. Furthermore, the region of flow acceleration stemming from the previous shed tip-vortex on the windward side appears lower compared to the previous plane. This is consistent with the vortex system described in Section 2 and the downward convection of the UW vortex. Finally, at the most downstream location $x/D = 1.60$ the wake has ejected further laterally while leaving a large region of high-speed flow within the frontal area of the rotor. The region of flow acceleration enclosed between the large-scale vortex and the wake has dissipated.

The negative pitch case $\beta = -10°$ shows a minimal flow deficit on the most upstream location of $x/D = 0.26$, with dominant regions following the shed vorticity of the blades. As described in Section 2, the load is shifted downstream for this pitch case. Hence, the wake has had less time to develop compared to the positive pitch case, where the load is shifted upwind and shows a weaker flow deficit compared to the zero pitch case. As in the positive pitch case, the presence of flow acceleration is evident on the leeward side of the rotor due to the high-strength tip vortex. At the cross-stream location $x/D = 0.90$, the wake has had more time to develop with a more pronounced flow deficit structure. Consistent with the vortex structures, the wake contracts laterally while ejecting axially above the actuator surface. This is clearly visible on the leeward half of the rotor, where a region of high-speed flow is present within the frontal area of the rotor while the wake is stretched above the surface. The magnitude of the flow acceleration on the leeward side of the rotor has seemingly grown as described in Section 4.2, the weaker UL vortex has convected inward, and the high-strength DL vortex has had more time to develop, making it the dominant feature on the

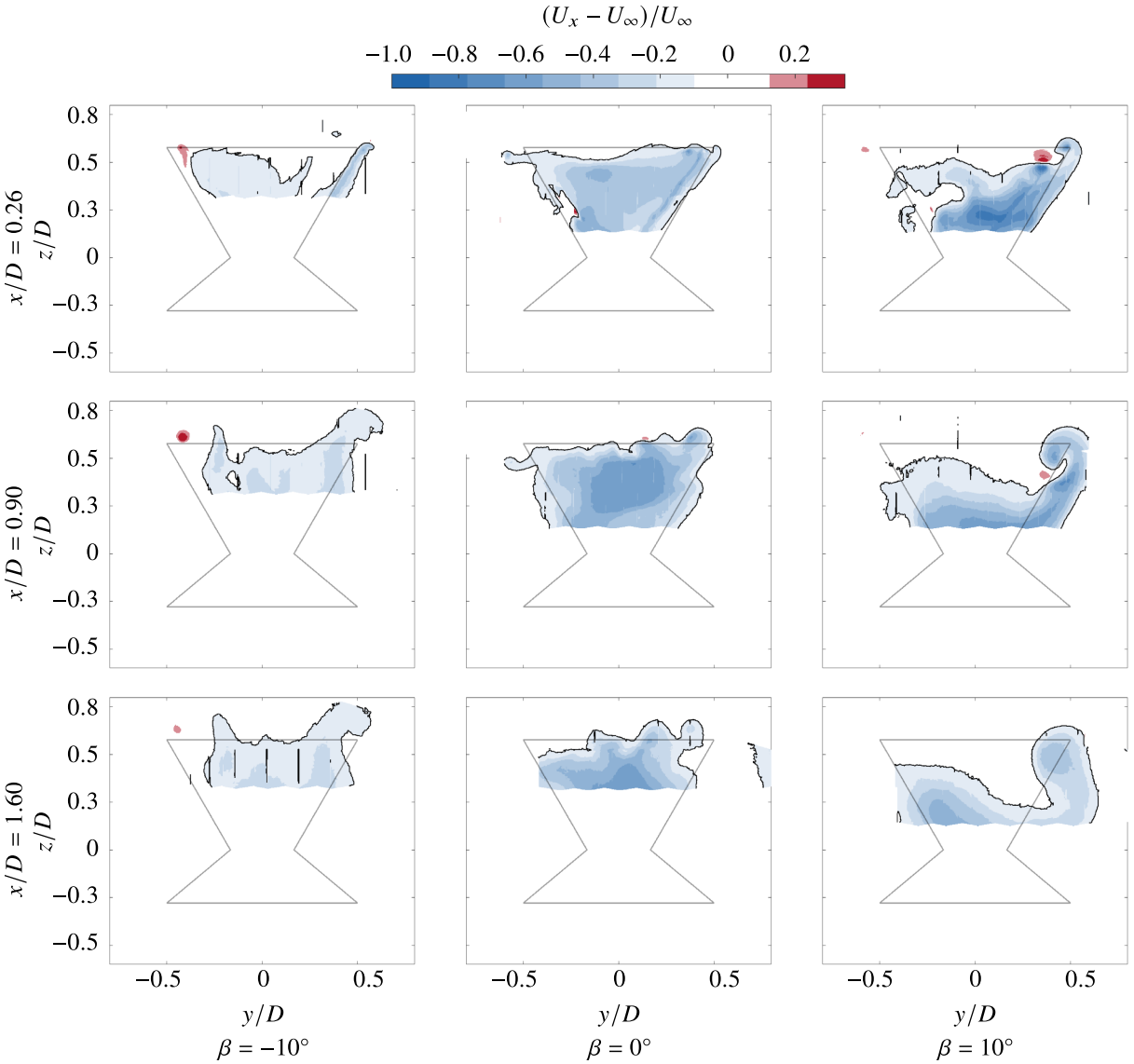

FIGURE 14 | Velocity deficit contours at cross-stream locations $x/D = 0.26$, 0.90, and 1.60 for fixed pitch cases $\beta = -10°$, 0°, and 10°. The gray line represents the frontal area of the rotor.

leeward side. Similarly, the wake on the windward half of the rotor is ejected above the frontal area due to the DW quadrant, consistent with the discussion in Section 2 and results in Section 4.2. Due to this upward convection of the tip-vortex, the flow deficit on the windward side of the rotor at heights around $z/D = 0.4$ is not contracting axially to the same degree as on the leeward side of the rotor. At the downstream location $x/D = 1.60$, the vortex on the DL quadrant has deformed the wake more with a larger area of high-speed flow present within the frontal area of the rotor. Contrarily, only a small region of high-speed flow is present on the windward side of the rotor near the blade tip.

4.4 | Phase-Locked Flow Fluctuations

The normalized standard deviation (SD) magnitude $|\sigma| = \sqrt{\sigma_u^2 + \sigma_w^2 + \sigma_v^2}/U_\infty$ where σ denotes the standard-deviation of the phase-locked velocity component, is plotted in Figure 15. Previous work [52] relied on a combination of phase-locked and time-averaged data to isolate mean, periodic, and random velocity terms. As no time-averaged results are available, the standard deviation term encompasses the quality of the phase-lock as well as local turbulent flows in the wake. The lack of time-averaged data hinders the isolation of these two components as done in previous works [26, 53]. However, as turbulent flow would lead to higher standard deviations, this approach succeeds in giving a relative indication of regions with unsteady flow separation and turbulence.

The first row shows $|\sigma|$ for the cross-stream plane $x/D = 0.26$. For the zero pitch case, SD magnitudes are highest at the edge of the wake. Large magnitudes are evident in the regions where coherent shed vorticity is present from the blade that has just passed, with slightly weaker values than those generated by the previous blade. A clear transition from attached

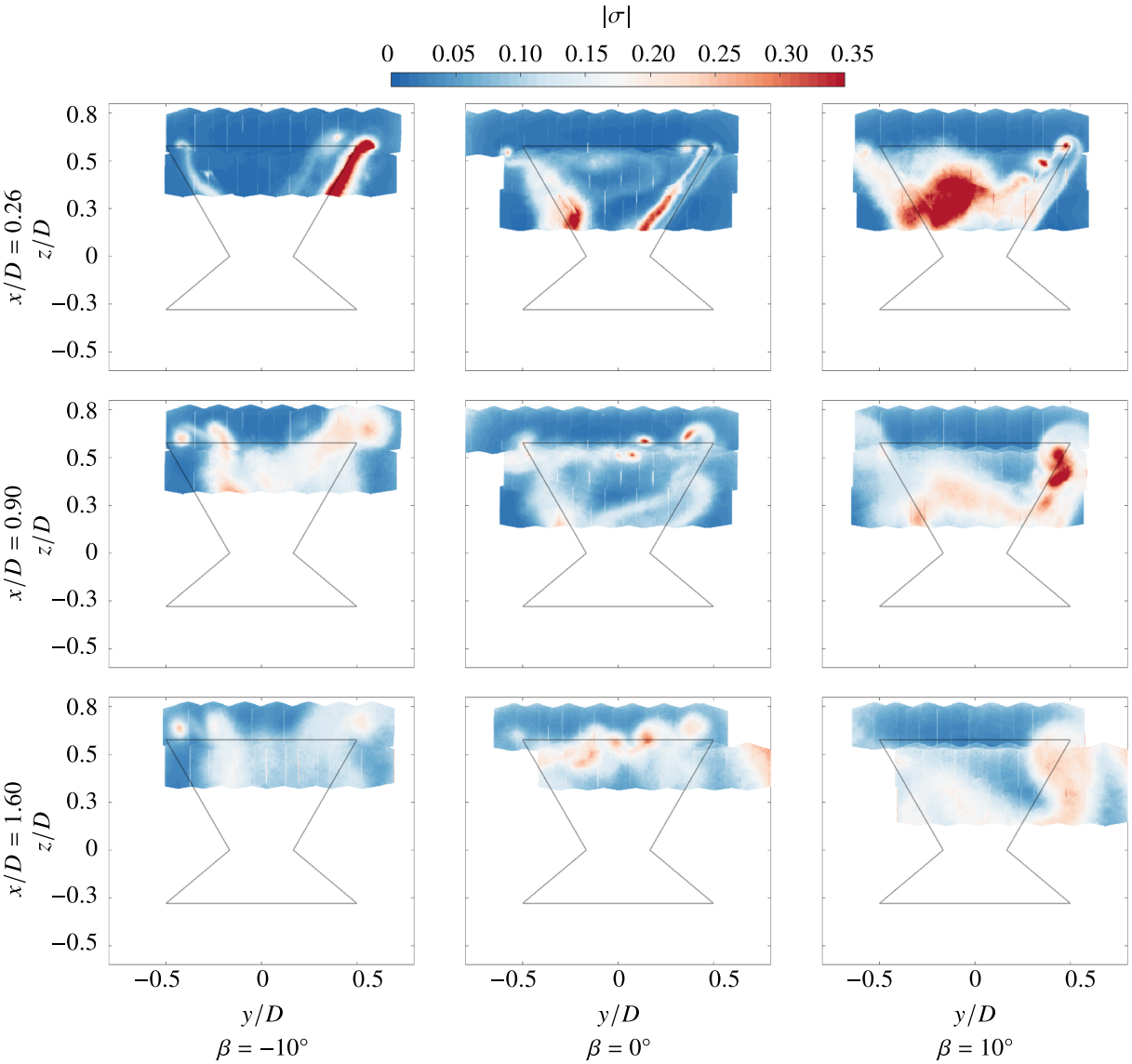

FIGURE 15 | Normalized standard deviation magnitude, $|\sigma|$, contours at cross-stream locations $x/D = 0.26$, 0.90, and 1.60 for fixed pitch cases $\beta = -10°$, 0°, and 10°. The gray line represents the frontal area of the rotor.

to separated flow is visible on the windward side of the rotor at around $z/R = 0.37$. This corresponds to a local tip-speed ratio of $\lambda = 3.0$. A similar separation region is evident on the leeward side of the rotor. For the positive pitch case $\beta = 10°$, moderate intensities are evident at the edges of the wake. The tip vortices have high magnitudes of SD, indicating some meandering of the vortex structures and hence smearing in the phase-lock. Furthermore, a large region of high SD is evident on the windward side of the rotor. This region corresponds to the intersection of the measurement plane of the generated shed vorticity from the blade passing through the UL quadrant of the cycle. As expected, the blade is heavily stalled in this region due to high magnitudes in relative angle of attack, specifically in regions moving towards the blade's root where the local tip-speed ratio decreases. For the negative pitch case, high magnitudes in SD are evident on the windward side of the rotor following the blade's trajectory. This is generated by the blade that just exited the DW quadrant of the cycle, where the angle of attack magnitudes are increased through the pitching action, presumably leading to stall. The shed vorticity of the previous blade generated in the UW quadrant appears at a lower magnitude and more inboard towards $y/D = 0$, as seen in Figure 12. The shed vorticity on the leeward side of the rotor is generated in the UL quadrant, where the angles of attack are systematically reduced through the pitching action, leading to more attached flow along the span of the blade.

The second row is at a cross-stream plane of $x/D = 0.9$. The zero pitch case shows peaks in SD at the tip vortices. Once again, moderate streaks of SD are apparent at the edge of the wake as well as along the shed vorticity of the blades. As this is now further in the wake, these structures have begun to diffuse and deform compared to the previous plane. The positive pitch case shows high standard deviation on the tip vortex as before, which has grown in size. As in the zero pitch case, high SD is not only concentrated along the perimeter of the wake but also quite dominant within. This can be attributed to shed vorticity structures that have convected downstream

generated by the blade in the UW quadrant. As in the previous plane, the blade is expected to be stalling here due to the systematic increase in the angle of attack across the span. The negative pitch case shows moderate intestines in SD along the deformed edge of the wake. The windward side of the rotor shows a presence of high SD within the wake, which can be attributed to the stalled blade of the DW quadrant that has convected downstream.

Finally, the third row shows the SD at cross-stream plane $x/D = 1.6$. The zero pitch case has moderate SD concentrated along the perimeter of the wake with high magnitudes concentrated around the mixing and diffusing tip-vortex structures. At the edge of the measurement domain, a path of high SD is evident where the edge of the open jet is reached. For the positive pitch case, the distribution looks the same as in the previous plane, with a decrease in magnitude due to diffusion. The negative pitch case shows similar behavior to the previous plane as well as the positive pitch case. Given the convective speed of U_∞ (without considering rotor induction) and the rotational frequency of 21.3 rad/s, the wake structure has convected approx. $x = 0.8$D in one cycle, explaining the similarity between the flow fields at $x/D = 0.9$ and 1.6.

4.5 | Momentum Recovery

The previous sections have described the vortex system of the X-Rotor as well as the subsequent impact on the wake shape. Previous studies [26, 52, 53] have highlighted the mechanism of streamwise momentum recovery in the wakes of rotors by considering the time-averaged Reynolds averaged Navier-Stokes equation. As the presented results in this study are phase-locked, the unsteady RANS equation for streamwise flow is presented in Equation (6) for a single phase in the periodic cycle of the wake.

$$\begin{aligned}\frac{\partial \overline{U}_x}{\partial t} = &-\overline{U}_x\frac{\partial \overline{U}_x}{\partial x} - \overline{U}_y\frac{\partial \overline{U}_x}{\partial y} - \overline{U}_z\frac{\partial \overline{U}_x}{\partial z} \\ &- \frac{1}{\rho}\frac{\partial \overline{p}}{\partial x} - \frac{\partial}{\partial x}\overline{u'_x u'_x} - \frac{\partial}{\partial y}\overline{u'_x u'_y} - \frac{\partial}{\partial z}\overline{u'_x u'_z}\end{aligned} \tag{6}$$

As in the aforementioned studies, the viscous terms are neglected due to the sufficiently high Reynolds number. The overlines and primes are the phase-locked means and fluctuating components, respectively. For this simplified analysis, the streamwise derivative terms ($\partial \overline{U}_x/\partial x$, $\partial \overline{u'_x u'_x}/\partial x$) and pressure term are not presented as they are not measured. Hence, in Equation (6), we consider only the instantaneous contributions of the advection and Reynolds stress terms in the lateral and axial directions to the streamwise advection in the wake. The advection terms in the lateral and axial direction are kept on the RHS to evaluate their impact on the streamwise advection (LHS).

The aforementioned terms of Equation (6) at a cross-stream plane $x/D = 0.9$ for the three fixed pitch cases are shown in Figure 16. The black contour line indicates where $U_x/U_\infty = 0.9$, and the gray line indicates the frontal area of the rotor. All terms are normalized by the turbine diameter and freestream flow component. Following the style of Huang et al. [26], positive (red) values have a favorable contribution to the wake recovery process and visa-versa.

The first row shows the lateral advection of streamwise momentum. For the baseline case of $\beta = 0°$, blue regions are present around the circumference of the wake edge, specifically on the windward side. This can be attributed to the expansion of the wake where low momentum flow is transported laterally outward from the wake center. Similarly, a large region of blue is evident at the edge of the wake for the positive pitch case due to the transport of low momentum flow from the wake, latterly outward. This is complemented by a red region on the windward side where the high momentum flow is injected laterally from the free stream flow above the rotor. The negative pitch case shows a similar trend of closely spaced red and blue regions on the leeward side of the rotor. The blue corresponds to low momentum flow being pushed axially inward from the edge of the wake, while free stream flow is injected laterally from the side of the rotor (red). The same mechanism is also present on the windward side of the rotor, albeit at a lower degree.

The second row shows the axial advection of streamwise momentum. For the baseline case, high magnitudes are mainly concentrated around the coherent tip-vortex structures, which are convecting downstream. For the positive pitch case, a large region of red is present along the upper edge of the wake and on the windward side of the rotor. This can be explained by the axial contraction of the wake due to the injection of free stream, that is, high momentum flow from above the rotor. The leeward side of the rotor shows lower magnitudes of vertical advection as expected by the lower strength tip-vortex and, subsequently, a lesser degree of wake deformation. The $\beta = -10°$ case shows a large presence of blue on the edge of the wake above the rotor. This indicates an advection of low momentum streamwise flow from the center of the wake axially outward. This is present on both the windward and leeward sides of the rotor and complimented by regions of red on the lateral edges of the wake. This indicates the high momentum flow is attributed to the vertical induction of the large-scale tip vertical structures.

The third and fourth rows present the Reynolds stress term distributions in the lateral and axial directions, respectively. Evident from a visual comparison between the top and bottom rows, the advection terms play a more dominant role in redistributing momentum in the wake, consistent with the results of Huang et al. [26].

To further highlight the impacts of fixed blade pitch on the wake re-energization, the axial advective component of the mean-kinetic energy (MKE) flux above the rotor is shown in Figure 17. The importance of vertical fluxes towards the replenishment of energy in farm arrays has been highlighted by Stevens and Meneveau [54]. A control volume approach is taken, as proposed by Hezaveh and Bou-Zeid [55], where the vertical fluxes above the rotor at $z/D = 0.7$ within the diameter of the rotor ($-0.5 < y/D < 0.5$) are computed. For typical HAWT farms, the dominant term is typically the turbulent-induced vertical flux. However, as concluded above, the advective component is more dominant in the wake re-energization procedure of the X-Rotor with pitched blades. As such, only the, only the advective flux of MKE $-0.5U_zU_x^2$ is presented, normalized by the freestream flow. The profile is extracted

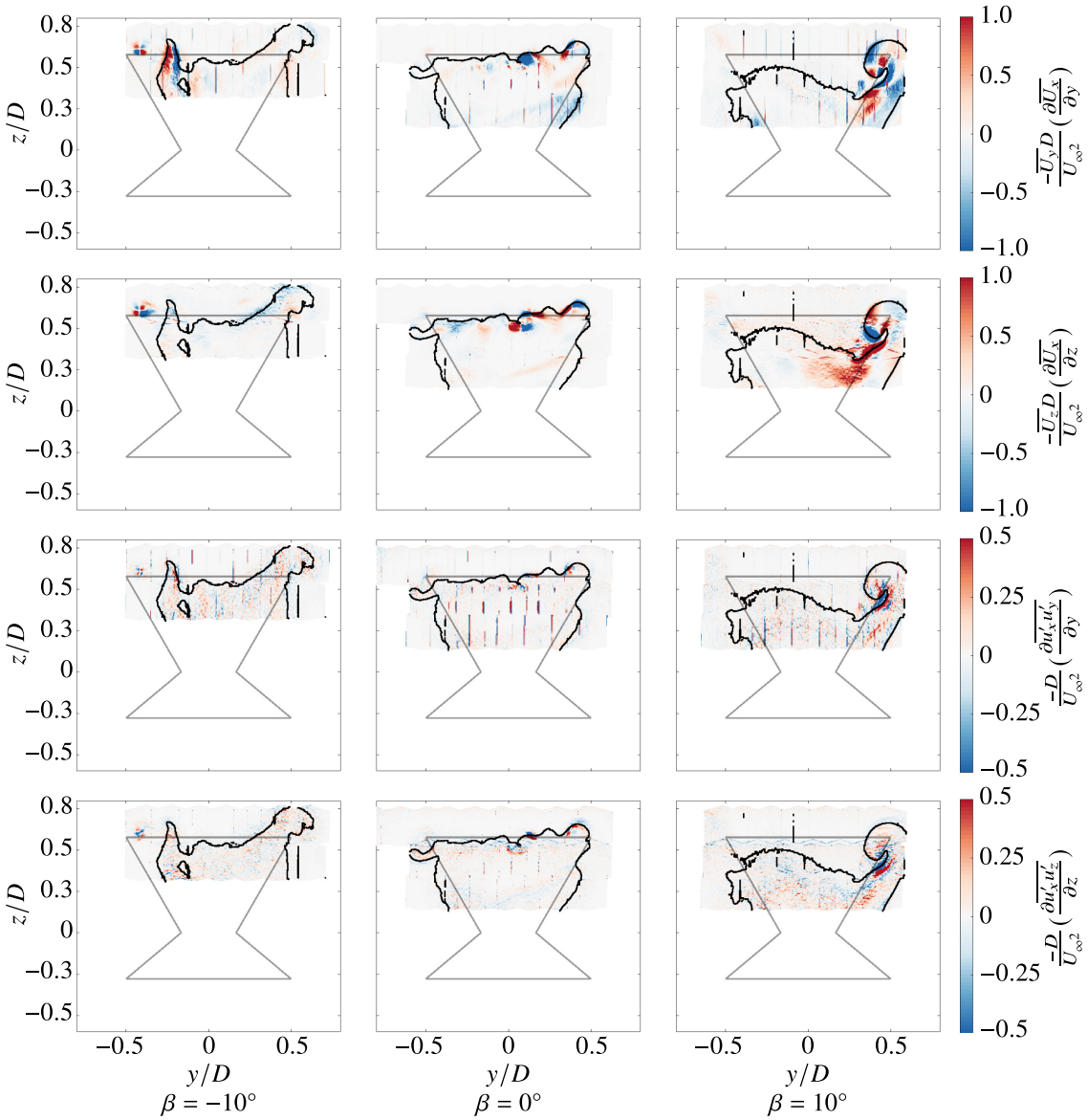

FIGURE 16 | Terms of Equation (6) for each fixed pitch case at wake position $x/D = 0.9$. For each case, the value is normalized by the ratio between turbine diameter and free stream velocity (D/U_∞^2).

over all cross-stream locations of the rotor. The mean profile is presented via a solid line with the shaded region representing the standard deviation across all cross-stream planes.

The axial MKE flux above the rotor does not change drastically as a function of cross-stream location across all pitch cases in these near-wake measurements. The pitch $\beta = 0°$ case shows a relatively flat curve around a zero magnitude flux, indicating minimal energy deleted[id=DB]momentum transfer above the rotor. Despite this, the mean curve does fall above zero on the leeward side due to the downwash of the vortex in the UL quadrant. Due to the asymmetry in the wake discussed in Section 4.3, the flux magnitude becomes negative on the windward side of the rotor. In this region, there is a higher magnitude of variety between the different cross-stream planes, as evidenced by the larger shaded area. As discussed in Section 4.1, the aforementioned asymmetry grows between the windward and leeward sides of the rotor when moving downstream.

The negative pitch case $\beta = -10°$ exhibits a predominantly negative axial flux magnitude across the entire diameter of the rotor. This is consistent with the impact of the vortex system on the wake topology, described in Section 4.2. The magnitude increases at the edge of the windward side due to the strong DW vortex which has convected above the rotor. Similarly, the magnitude is positive for a small portion on the leeward side of the rotor due to the DL vortex which has convected inward towards $y/D = 0$. More significant variations as a function of cross-stream location are apparent at the regions near the dominant vortices due to the time taken for the structures to form, as discussed in Section 4.2.

Finally, the pitch case $\beta = 10°$ shows a consistent positive magnitude in flux, signifying a downwash. The downwash magnitude is significantly higher on the windward side of the rotor due to the UW vortex's higher strength than the UL, as highlighted in Figure 13. As a result, the flux magnitudes on the windward side are high before decreasing when moving towards the leeward side of the rotor. Unlike the aforementioned pitch cases,

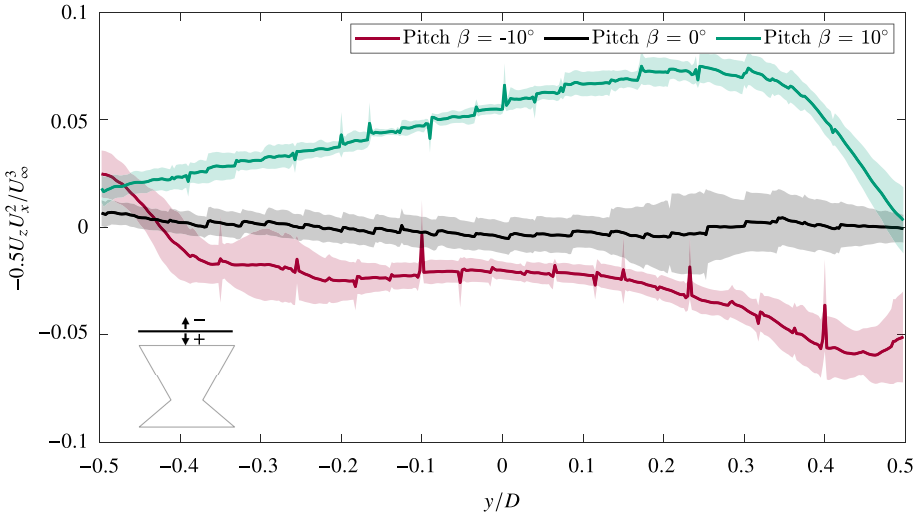

FIGURE 17 | Normalized axial advective MKE flux $-0.5U_zU_x^2/U_\infty^3$ through a line at $z/D = 0.7$ within the diameter of the rotor ($-0.5 < y/D < 0.5$) at cross-stream locations $0.26 < x/D < 1.6$ for the three pitch cases. The mean profile across all cross-stream locations is shown via a solid line and a shaded area signifying the standard deviation. The icon at the bottom left of the figure illustrates the line through which the flux is considered, with the respective positive and negative directions marked.

minor variation as a function of cross-stream location is apparent. As the positive pitch case is an upwind phenomenon discussed in Section 4.2, the vortex system is already established when measuring downstream. The positive pitch case has a higher magnitude in axial MKE flux on average across the rotor diameter, with $< -0.5U_zU_x^2/U_\infty^3 > = 0.05$ compared to -0.03 and 0 for the negative and zero pitch settings, respectively.

5 | Conclusions

The role of the X-Rotor's loading on the wake topology is defined using the AC theory and further validated using the CACTUS numerical model. The numerically obtained angle of attack distribution across the X-Rotor's upper blades and subsequent azimuthally resolved loading confirm the impacts of fixed blade pitch on the load distribution of the X-Rotor. This working principle is further validated and demonstrated through an experimental study of the near wake of a scaled X-Rotor using stereoscopic PIV measurements. The results confirm the theoretical load distribution modifications realized by fixed-blade pitch and align with previous works that theoretically defined and demonstrated the impact of fixed-blade pitch on an H-Type VAWT.

The velocity components and the streamwise vorticity in the wake reveal two distinct modes of operation. For the positive pitch case (pitched in), the strength of the upwind vortex is dominant, leading to flow entrainment axially from the free stream complimented by an ejection of the wake in the lateral direction. Conversely, for the negative pitch case (pitched out), the strength of the downwind vortex is dominant, leading to an opposing direction of rotation and, subsequently, a wake ejection axially upward and flow entrainment laterally from the sides. The standard deviation of the phase-locked flow fields shed light on regions where the blade is presumably stalling along the coned span due to the local differences in tip-speed ratio. Further, the change in effective angle of attack through fixed-blade pitch also triggers stall onset in certain quadrants of the rotor's motion as the stall angle is surpassed. A comparison of the flowfield with the theoretical blade integrated load distribution confirms this behavior. Finally, an analysis of the in-plane advection terms of the streamwise velocity confirms the wake re-energizing mechanism of the X-Rotor, highlighting the constructive induction of the large-scale tip vortices on momentum recovery.

The presented results highlight the streamwise vorticity system's critical role in the momentum transfer in the wake of the X-Rotor VAWT. Further, this mechanically simple wake control mechanism of fixed blade pitch would yield huge potential for farm-scale installation of X-Rotor VAWTs due to the aforementioned benefits in wake recovery. Future work will focus on studying the far wake of the X-Rotor with fixed blade pitch to further demonstrate the potential for farm-scale installation. Furthermore, an array of X-Rotor VAWTs will be tested to investigate the wake-wake and wake-rotor interactions with fixed blade pitch. Additionally, studies will be conducted to quantify the trade-off between wake recovery and subsequent increased power capture of downstream turbines versus the performance loss of individual turbines with fixed blade pitch. Finally, the presented results serve as a benchmark for the validating numerical models being developed in parallel for the X-Rotor. These models need to capture the strong three-dimensionality of the flowfield resulting from the coned nature of the blades and the complex vortex system generated by the blade tips and root regions of the geometry.

Acknowledgments

We wish to acknowledge the great help of Ed Roessen, Rob van der List, and Eddy van den Bos for their support with the design and fabrication of the experimental models used in this study.

Data Availability Statement

The data supporting this study's findings are openly available in 4TU ResearchData at https://doi.org/10.4121/e43ddd4d-6d93-4f50-b1ce-01bc0df1bda4.

Peer Review

The peer review history for this article is available at https://www.webofscience.com/api/gateway/wos/peer-review/10.1002/we.2944.

References

1. J. Wang, S. Qin, S. Jin, and J. Wu, "Estimation Methods Review and Analysis of Offshore Extreme Wind Speeds and Wind Energy Resources," *Renewable and Sustainable Energy Reviews* 42 (2015): 26–42.

2. M. D. Esteban, J. J. Diez, J. S. López, and V. Negro, "Why Offshore Wind Energy?," *Renewable Energy* 36, no. 2 (2011): 444–450.

3. P. K. Chaviaropoulos, A. Natarajan, and P. H. Jensen, "Key Performance Indicators and Target Values for Multi-Megawatt Offshore Turbines," *European Wind Energy Conference*, (2014).

4. E. J. D. E.C.M. Ruijgrok and B. H. Bulder, "Cost Evaluation of North Sea Offshore Wind Post 2030," TNO, Witteveen+Bos Raadgevende ingenieurs B.V. Leeuwenbrug 8, P.O. Box 233, 7400 AE Deventer, The Netherlands, (2019).

5. S. C. Pryor, R. J. Barthelmie, T. J. Shepherd, A. N. Hahmann, and O. M. G. Santiago, "Wakes in and Between Very Large Offshore Arrays," *Journal of Physics: Conference Series* 2265, no. 2 (2022): 22037, https://doi.org/10.1088/1742-6596/2265/2/022037.

6. P. Fleming, J. Annoni, J. J. Shah, et al., "Field Test of Wake Steering at an Offshore Wind Farm," *Wind Energy Science* 2, no. 1 (2017): 229–239.

7. M. F. Howland, S. K. Lele, and J. O. Dabiri, "Wind Farm Power Optimization Through Wake Steering," *Proceedings of the National Academy of Sciences* 116, no. 29 (2019): 14495–14500.

8. R. J. Barthelmie, K. Hansen, S. T. Frandsen, et al., "Modelling and Measuring Flow and Wind Turbine Wakes in Large Wind Farms Offshore," *Wind Energy: An International Journal for Progress and Applications in Wind Power Conversion Technology* 12, no. 5 (2009): 431–444.

9. J. K. Lundquist, K. K. DuVivier, D. Kaffine, and J. M. Tomaszewski, "Costs and Consequences of Wind Turbine Wake Effects Arising From Uncoordinated Wind Energy Development," *Nature Energy* 4, no. 1 (2019): 26–34.

10. D. R. Houck, "Review of Wake Management Techniques for Wind Turbines," *Wind Energy* 25, no. 2 (2022): 195–220.

11. F. Porté-Agel, M. Bastankhah, and S. Shamsoddin, "Wind-Turbine and Wind-Farm Flows: A Review," *Boundary-layer meteorology* 174 (2020): 1–59.

12. M. Bastankhah and F. Porté-Agel, "Wind Farm Power Optimization via Yaw Angle Control: A Wind Tunnel Study," *Journal of Renewable and Sustainable Energy* 11, no. 2 (2019): 23301.

13. D. Bensason, E. Simley, O. Roberts, et al., "Evaluation of the Potential for Wake Steering for US Land-Based Wind Power Plants," *Journal of Renewable and Sustainable Energy* 13, no. 3 (2021): 33303.

14. P. Fleming, J. King, K. Dykes, et al., "Initial Results From a Field Campaign of Wake Steering Applied at a Commercial Wind Farm—Part 1," *Wind Energy Science* 4, no. 2 (2019): 273–285.

15. S. Mertens, G. van Kuik, and G. van Bussel, "Performance of an H-Darrieus in the Skewed Flow on a Roof," *Journal of Solar Energy Engineering* 125, no. 4 (2003): 433–440.

16. A. Buchner, J. Soria, D. Honnery, and A. Smits, "Dynamic Stall in Vertical Axis Wind Turbines: Scaling and Topological Considerations," *Journal of Fluid Mechanics* 841 (2018): 746–766.

17. S. Jain and U. Saha, "The State-of-the-Art Technology of H-Type Darrieus Wind Turbine Rotors," *Journal of Energy Resources Technology* 142, no. 3 (2019): 30801.

18. D. T. Griffith, J. Paquette, M. Barone, et al., "A Study of Rotor and Platform Design Trade-Offs for Large-Scale Floating Vertical Axis Wind Turbines," *Journal of Physics: Conference Series* 753, no. 10 (2016): 102003, https://doi.org/10.1088/1742-6596/753/10/102003.

19. R. Whittlesey, S. Liska, and J. Dabiri, "Fish Schooling as a Basis for Vertical Axis Wind Turbine Farm Design," *Bioinspiration & Biomimetics* 5, no. 2 (2010): 35005.

20. J. Dabiri, "Potential Order-of-Magnitude Enhancement of Wind Farm Power Density via Counter-Rotating Vertical-Axis Wind Turbine Arrays," *Journal of Renewable and Sustainable Energy* 3, no. 4 (2011): 43104.

21. M. Kinzel, Q. Mulligan, and J. O. Dabiri, "Energy Exchange in an Array of Vertical-Axis Wind Turbines," *Journal of Turbulence* 13, no. 1 (2012): N38.

22. J. Bremseth and K. Duraisamy, "Computational Analysis of Vertical Axis Wind Turbine Arrays," *Theoretical and Computational Fluid Dynamics* 30 (2016): 387–401.

23. G. Tescione, D. Ragni, C. He, C. Simao Ferreira, and G. G. van Bussel, "PIV-Based Analysis of 2D and 3D Flow Phenomena of Vertical Axis Wind Turbine Aerodynamics," in *32nd ASME Wind Energy Symposium*, (2014), 1080.

24. N. J. Wei, I. D. Brownstein, J. L. Cardona, M. F. Howland, and J. O. Dabiri, "Near-Wake Structure of Full-Scale Vertical-Axis Wind Turbines," *Journal of Fluid Mechanics* 914 (2021): A17.

25. K. J. Ryan, F. Coletti, C. J. Elkins, J. O. Dabiri, and J. K. Eaton, "Three-Dimensional Flow Field Around and Downstream of a Subscale Model Rotating Vertical Axis Wind Turbine," *Experiments in Fluids* 57 (2016): 1–15.

26. M. Huang, A. Sciacchitano, and C. Ferreira, "On the Wake Deflection of Vertical Axis Wind Turbines by Pitched Blades," *Wind Energy* 26, no. 4 (2023): 365–387.

27. P. Ouro, S. Runge, Q. Luo, and T. Stoesser, "Three-Dimensionality of the Wake Recovery Behind a Vertical Axis Turbine," *Renewable Energy* 133 (2019): 1066–1077.

28. D. B. Araya, T. Colonius, and J. O. Dabiri, "Transition to Bluff-Body Dynamics in the Wake of Vertical-Axis Wind Turbines," *Journal of Fluid Mechanics* 813 (2017): 346–381.

29. M. Huang, C. Ferreira, A. Sciacchitano, and F. Scarano, "Wake Scaling of Actuator Discs in Different Aspect Ratios," *Renewable Energy* 183 (2022): 866–876.

30. M. Huang, C. Ferreira, A. Sciacchitano, and F. Scarano, "Experimental Comparison of the Wake of a Vertical Axis Wind Turbine and Planar Actuator Surfaces," *Journal of Physics: Conference Series* 1618 (2020): 52063.

31. A. E. Craig, J. O. Dabiri, and J. R. Koseff, "Low Order Physical Models of Vertical Axis Wind Turbines," *Journal of Renewable and Sustainable Energy* 9, no. 1 (2017): 13306.

32. D. De Tavernier, C. Ferreira, U. Paulsen, and H. Madsen, "The 3D Effects of a Vertical-Axis Wind Turbine: Rotor and Wake Induction," *Journal of Physics: Conference Series* 1618 (2020): 52040.

33. L. Massie, P. Ouro, T. Stoesser, and Q. Luo, "An Actuator Surface Model to Simulate Vertical Axis Turbines," *Energies* 12, no. 24 (2019): 4741.

34. V. Mendoza and A. Goude, "Improving Farm Efficiency of Interacting Vertical-Axis Wind Turbines Through Wake Deflection Using Pitched Struts," *Wind Energy* 22, no. 4 (2019): 538–546.

35. W. Leithead, A. Camciuc, A. K. Amiri, and J. Carroll, "The X-Rotor Offshore Wind Turbine Concept," *Journal of Physics: Conference Series* 1356 (2019): 12031.

36. C. Flannigan, J. Carroll, and W. Leithead, "Operations Expenditure Modelling of the X-Rotor Offshore Wind Turbine Concept," *Journal of Physics: Conference Series* 2265 (2022): 32054.

37. D. Bensason, A. Sciacchitano, and C. Ferreira, "Near Wake of the X-Rotor Vertical-Axis Wind Turbine," *Journal of Physics: Conference Series* 2505 (2023): 12040.

38. L. Morgan and W. Leithead, "Aerodynamic Modelling of a Novel Vertical Axis Wind Turbine Concept," *Journal of Physics: Conference Series* 2257, no. 1 (2022): 12001, https://doi.org/10.1088/1742-6596/2257/1/012001.

39. A. Giri Ajay, L. Morgan, Y. Wu, et al., "Aerodynamic Model Comparison for an X-Shaped Vertical-Axis Wind Turbine," *Wind Energy Science Discussions* 2023 (2023): 1–25.

40. D. D. Tavernier, C. Ferreira, U. Paulsen, and H. Madsen, "The 3D Effects of a Vertical-Axis Wind Turbine: Rotor and Wake Induction," *Journal of Physics: Conference Series* 1618, no. 5 (2020): 52040, https://doi.org/10.1088/1742-6596/1618/5/052040.

41. B. LeBlanc and C. Simao Ferreira, "Experimental Demonstration of Thrust vectoring With a Vertical Axis Wind Turbine Using Normal Load Measurements," *Journal of Physics: Conference Series* 1618 (2020): 52030.

42. H. A. Madsen, "The Actuator Cylinder—A Flow Model for Vertical Axis Wind Turbines" (Ph.D. Thesis, Aalborg University, Denmark, 1983).

43. B. LeBlanc and C. Ferreira, "Estimation of Blade Loads for a Variable Pitch Vertical Axis Wind Turbine With Strain Gage Measurements," *Wind Energy* 25, no. 6 (2022): 1030–1045, https://onlinelibrary.wiley.com/doi/abs/10.1002/we.2713.

44. L. E. M. Lignarolo, D. Ragni, C. Krishnaswami, Q. Chen, C. J. S. Ferreira, and G. J. W. Van Bussel, "Experimental Analysis of the Wake of a Horizontal-Axis Wind-Turbine Model," *Renewable Energy* 70 (2014): 31–46.

45. B. LeBlanc and C. Simao Ferreira, "Overview and Design of Pitch-VAWT: Vertical Axis Wind Turbine With Active Variable Pitch for Experimental and Numerical Comparison," in *2018 Wind Energy Symposium*, (2018), 1243.

46. M. Raffel, C. E. Willert, F. Scarano, C. J. Kähler, S. T. Wereley, and J. Kompenhans, *Particle Image Velocimetry: A Practical Guide* (Springer, 2018).

47. J. Murray and M. Barone, "The Development of CACTUS, a Wind and Marine Turbine Performance Simulation Code," in *49th AIAA Aerospace Sciences Meeting including the New Horizons Forum and Aerospace Exposition*, (2011), 147.

48. M. Drela, "Xfoil: An Analysis and Design System for Low Reynolds Number Airfoils," in *Low Reynolds Number Aerodynamics: Proceedings of the Conference Notre Dame*, (Indiana, USA: Springer, 1989), 1–12.

49. A. Sciacchitano and F. Scarano, "Elimination of PIV Light Reflections via a Temporal High Pass Filter," *Measurement Science and Technology* 25, no. 8 (2014): 84009.

50. A. Sciacchitano and B. Wieneke, "PIV Uncertainty Propagation," *Measurement Science and Technology* 27, no. 8 (2016): 84006.

51. C. Simao Ferreira, C. Hofemann, K. Dixon, G. Van Kuik, and G. Van Bussel, "3-D Wake Dynamics of the VAWT: Experimental and Numerical Investigation," in *48th AIAA Aerospace Sciences Meeting Including the New Horizons Forum and Aerospace Exposition*, (2010), 643.

52. L. E. M. Lignarolo, D. Ragni, F. Scarano, C. J. S. Ferreira, and G. J. W. Van Bussel, "Tip-Vortex Instability and Turbulent Mixing in Wind-Turbine Wakes," *Journal of Fluid Mechanics* 781 (2015): 467–493.

53. J. Bossuyt, C. Meneveau, and J. Meyers, "Wind Farm Power Fluctuations and Spatial Sampling of Turbulent Boundary Layers," *Journal of Fluid Mechanics* 823 (2017): 329–344.

54. R. J. A. M. Stevens and C. Meneveau, "Flow Structure and Turbulence in Wind Farms," *Annual Review of Fluid Mechanics* 49 (2017): 311–339.

55. S. H. Hezaveh and E. Bou-Zeid, "Mean Kinetic Energy Replenishment Mechanisms in Vertical-Axis Wind Turbine Farms," *Physical Review Fluids* 3, no. 9 (2018): 94606.

Appendix A

Airfoil Polar

The XFOIL statically simulated polar for the NACA0021 blade used in the numerical demonstration of the load distribution in Section 3.5 is shown in Figure A1. The tabulated data for the polar is made available in the data repository Section 5. In this case, the static stall angle is taken as the point where the linear behavior between the lift and angle of attack ends, at $\alpha_{ss} = 9.1°$, with C_L =1.02. Beyond this point, the lift continues to increase in a non-linear fashion, reaching a maximum lift of $C_L = 1.1$ at $\alpha_{ss} = 17°$.

Appendix B

Isometric View of Velocity and Vorticity Fields

As discussed in Section 4.1, an isometric view of the complete set of measured fields in the wake is provided in Figures B1–B3. The frontal area of the rotor is shown with a gray line at azimuth $\theta = 0°$ with a black contour line outlining the wake at $U_x/U_\infty = 0.9$. The cross-stream planes for the pitch case $\beta = 0°$ are x/D = [0.26, 0.4, 0.5, 0.6, 0.7 0.8, 0.9, 1.0, 1.1, 1.2, 1.4,1.6]. The cross-stream planes for the pitch case $\beta = -10°$ are x/D = [0.26, 0.5, 0.6, 0.7, 0.9, 1.0, 1.2, 1.4, 1.6]. The cross-stream planes for the pitch case $\beta = 10°$ are x/D = [0.26, 0.4, 0.5, 0.7, 0.9, 1.0, 1.2, 1.4, 1.6].

The normalized streamwise vorticity fields are shown in Figure B4. Consistent with the results of Huang et al. [26] and the wake mechanism described in Section 2, the streamwise vorticity is dominated by the tip-vortices. Within the rotor's rotation volume ($x/D \leq 0.5$), there is also the presence of shed vorticity of the coned blade [37]. For the $\beta = 0°$ pitch case, coherent vortical structures are evident in the near wake shed from the respective blade and quadrants before mixing and diffusing around $x/D = 1$. The rotation directions of the tip-vortices for the pitched cases are consistent with their induced flows discussed in Section 4.1.

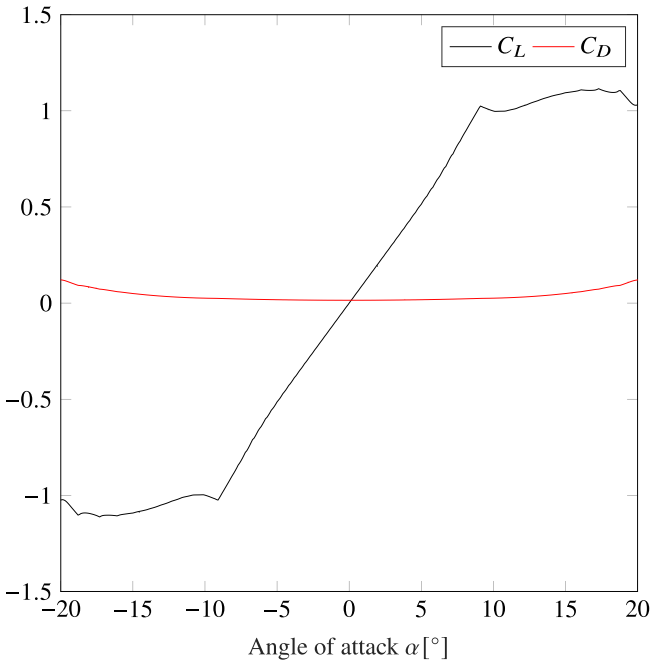

FIGURE A1 | Simulated NACA0021 polar using XFOIL at a Reynolds number of 15×10^4. The lift and drag coefficients C_L and C_D, respectively, are presented between angles of attack $-20° \leq \alpha \leq 20°$.

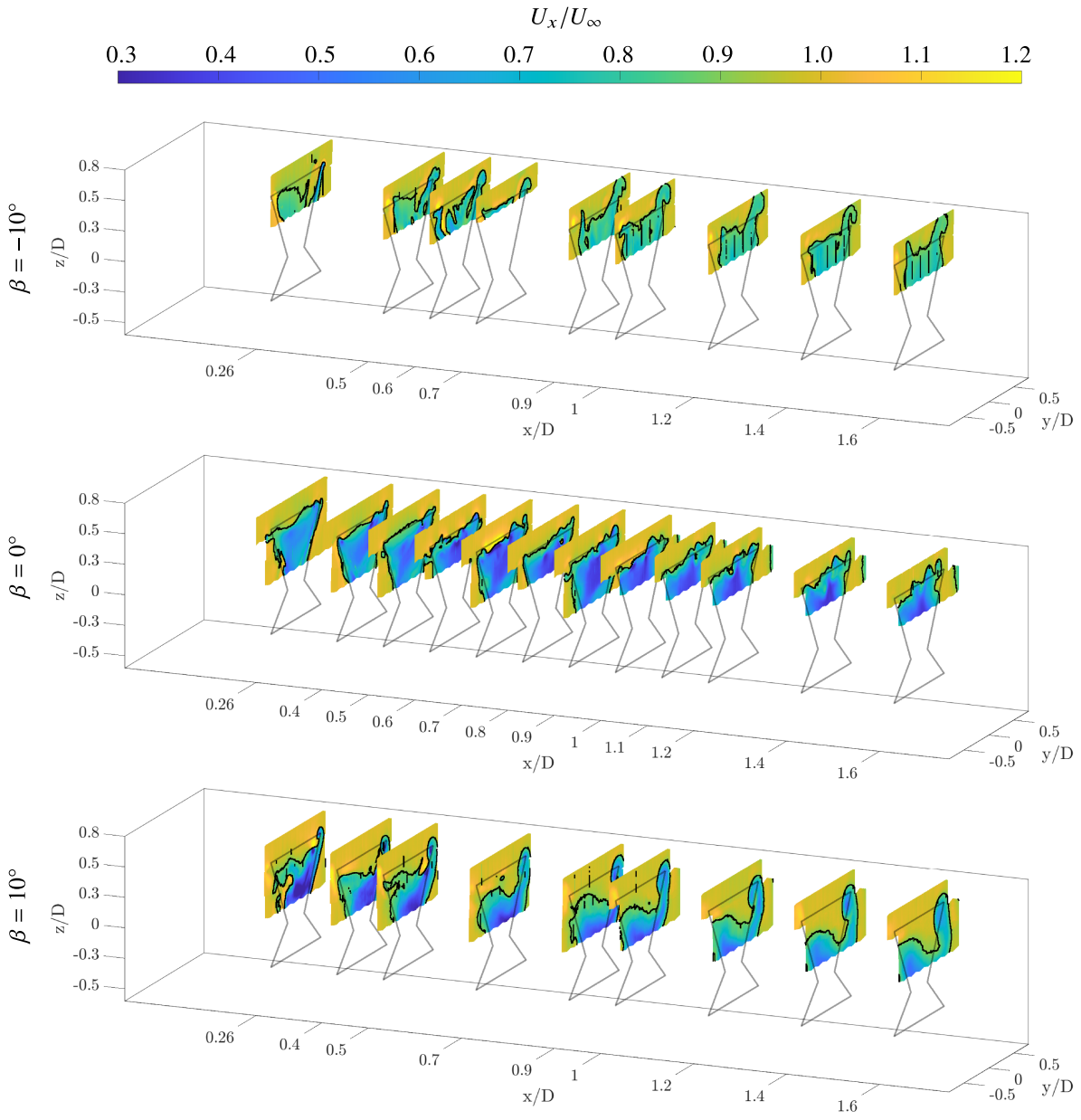

FIGURE B1 | Normalized streamwise flow (U_x/U_∞) at discrete cross-stream planes. The black solid line shows the frontal area of the rotor at an azimuth of 0° with a black contour line showing where $U_x/U_\infty = 0.9$. The scale in the streamwise direction is doubled to have the planes more spaced apart for observation.

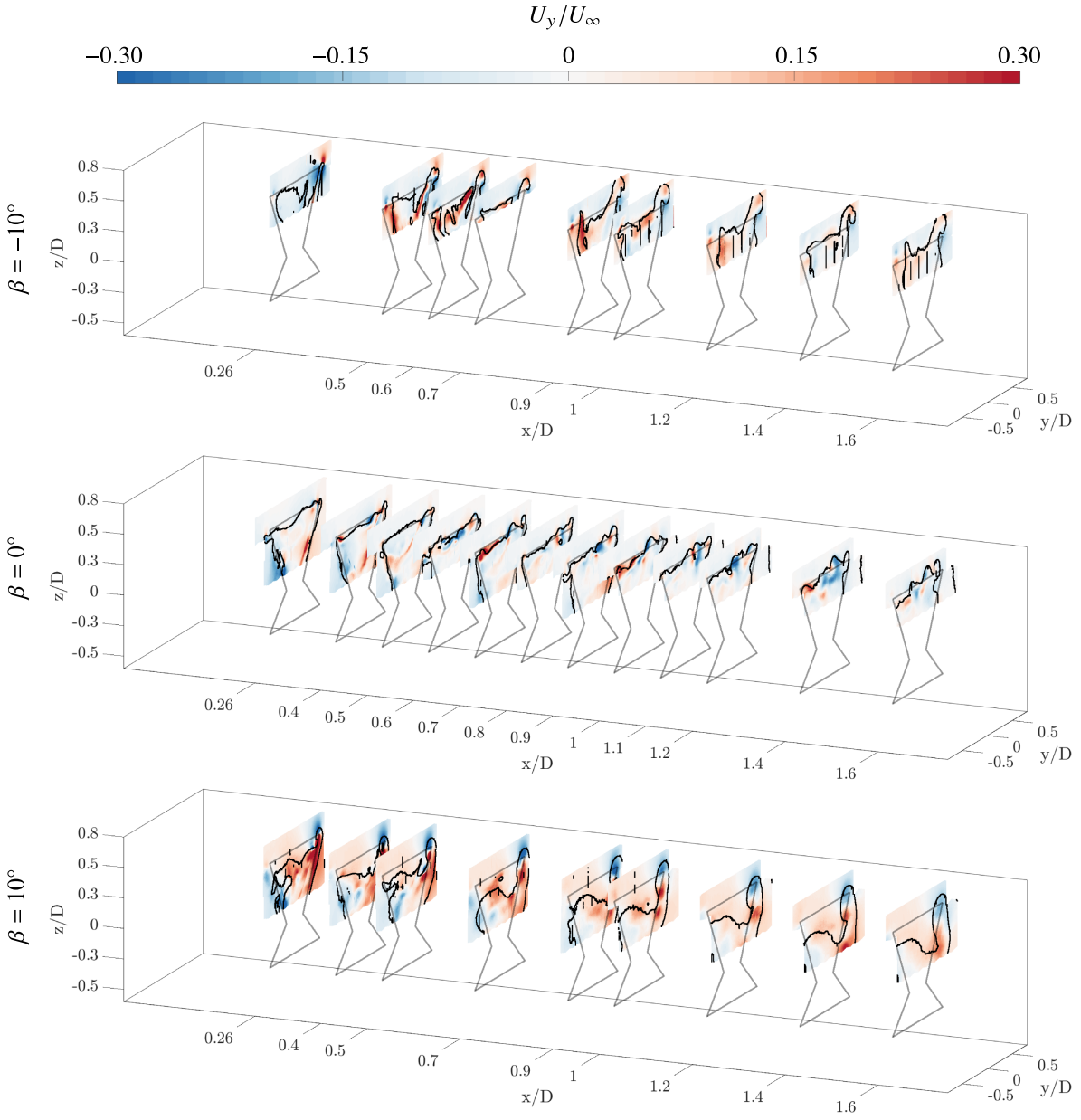

FIGURE B2 | Normalized lateral flow (U_y/U_∞) at discrete cross-stream planes. The black solid line shows the frontal area of the rotor at an azimuth of 0° with a black contour line showing where $U_x/U_\infty = 0.9$. The scale in the streamwise direction is doubled to have the planes more spaced apart for observation.

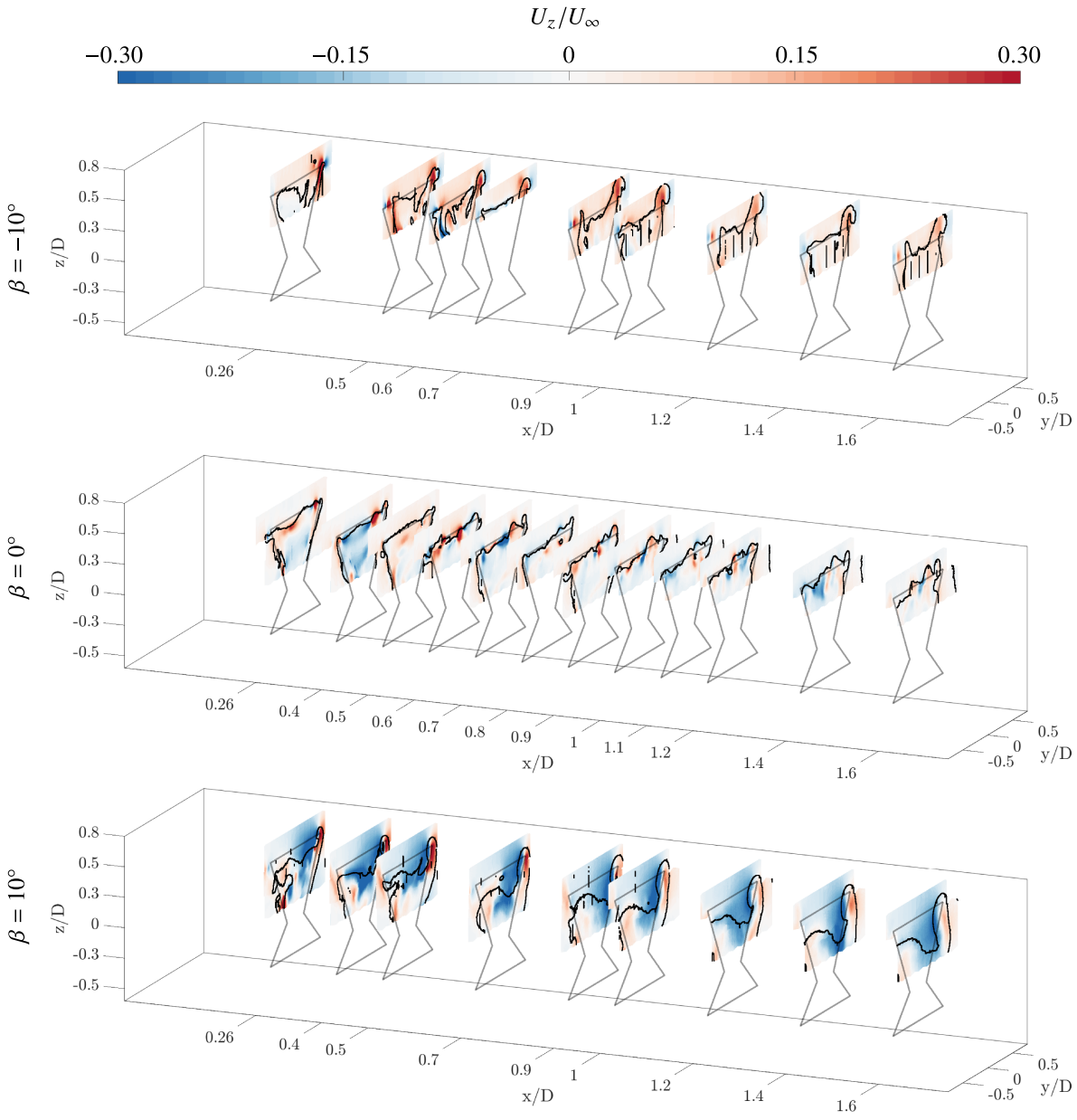

FIGURE B3 | Normalized axial flow (U_z/U_∞) at discrete cross-stream planes. The black solid line shows the frontal area of the rotor at an azimuth of 0° with a black contour line showing where $U_x/U_\infty = 0.9$. The scale in the streamwise direction is doubled to have the planes more spaced apart for observation.

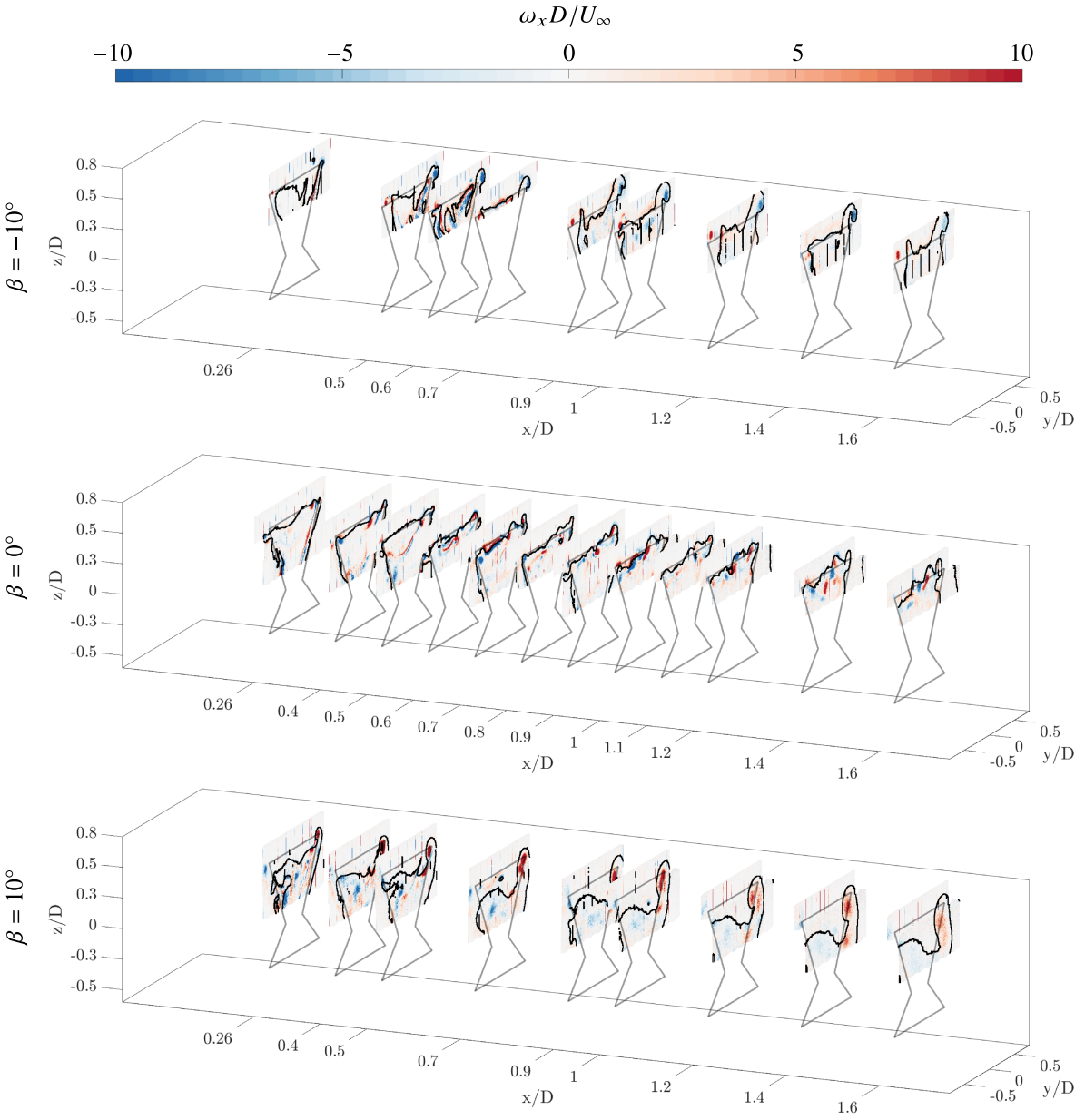

FIGURE B4 | Normalized streamwise vorticity ($\omega_x D/U_\infty$) at discrete cross-stream planes. The black solid line shows the frontal area of the rotor at an azimuth of 0° with a black contour line showing where $U_x/U_\infty = 0.9$.